

Bottlenecks to interstellar sulfur chemistry

Sulfur-bearing hydrides in UV-illuminated gas and grains

J. R. Goicoechea¹, A. Aguado², S. Cuadrado¹, O. Roncero¹, J. Pety³, E. Bron⁴, A. Fuente⁵, D. Riquelme⁶,
 E. Chapillon^{3,7}, C. Herrera³, and C. A. Duran^{6,8}

¹ Instituto de Física Fundamental (CSIC). Calle Serrano 121-123, 28006 Madrid, Spain
 e-mail: javier.r.goicoechea@csic.es

² Facultad de Ciencias. Universidad Autónoma de Madrid, 28049 Madrid, Spain

³ Institut de Radioastronomie Millimétrique (IRAM), Grenoble, France

⁴ LERMA, Observatoire de Paris, PSL Research University, CNRS, Sorbonne Universités, 92190 Meudon, France

⁵ Observatorio Astronómico Nacional (OAN), Alfonso XII, 3, 28014 Madrid, Spain

⁶ Max-Planck-Institut für Radioastronomie, Auf dem Hügel 69, 53121 Bonn, Germany

⁷ OASU/LAB-UMR5804, CNRS, Université Bordeaux, 33615 Pessac, France

⁸ European Southern Observatory, Alonso de Cordova 3107, Vitacura, Santiago, Chile

Received 25 October 2020 / Accepted 23 December 2020

ABSTRACT

Hydride molecules lie at the base of interstellar chemistry, but the synthesis of sulfuretted hydrides is poorly understood and their abundances often crudely constrained. Motivated by new observations of the Orion Bar photodissociation region (PDR) – 1'' resolution ALMA images of SH⁺; IRAM 30 m detections of bright H₂³²S, H₂³⁴S, and H₂³³S lines; H₃S⁺ (upper limits); and SOFIA/GREAT observations of SH (upper limits) – we perform a systematic study of the chemistry of sulfur-bearing hydrides. We self-consistently determine their column densities using coupled excitation, radiative transfer as well as chemical formation and destruction models. We revise some of the key gas-phase reactions that lead to their chemical synthesis. This includes ab initio quantum calculations of the vibrational-state-dependent reactions SH⁺ + H₂(*v*) ⇌ H₂S⁺ + H and S + H₂(*v*) ⇌ SH + H. We find that reactions of UV-pumped H₂(*v* ≥ 2) molecules with S⁺ ions explain the presence of SH⁺ in a high thermal-pressure gas component, $P_{\text{th}}/k \approx 10^8 \text{ cm}^{-3} \text{ K}$, close to the H₂ dissociation front (at $A_V < 2 \text{ mag}$). These PDR layers are characterized by no or very little depletion of elemental sulfur from the gas. However, subsequent hydrogen abstraction reactions of SH⁺, H₂S⁺, and S atoms with vibrationally excited H₂, fail to form enough H₂S⁺, H₃S⁺, and SH to ultimately explain the observed H₂S column density ($\sim 2.5 \times 10^{14} \text{ cm}^{-2}$, with an ortho-to-para ratio of 2.9 ± 0.3 ; consistent with the high-temperature statistical value). To overcome these bottlenecks, we build PDR models that include a simple network of grain surface reactions leading to the formation of solid H₂S (s-H₂S). The higher adsorption binding energies of S and SH suggested by recent studies imply that S atoms adsorb on grains (and form s-H₂S) at warmer dust temperatures ($T_d < 50 \text{ K}$) and closer to the UV-illuminated edges of molecular clouds. We show that everywhere s-H₂S mantles form(ed), gas-phase H₂S emission lines will be detectable. Photodesorption and, to a lesser extent, chemical desorption, produce roughly the same H₂S column density (a few 10^{14} cm^{-2}) and abundance peak (a few 10^{-8}) nearly independently of n_H and G_0 . This agrees with the observed H₂S column density in the Orion Bar as well as at the edges of dark clouds without invoking substantial depletion of elemental sulfur abundances.

Key words. astrochemistry – line: identification – ISM: clouds – photon-dominated region

1. Introduction

Hydride molecules play a pivotal role in interstellar chemistry (e.g., Gerin et al. 2016), being among the first molecules to form in diffuse interstellar clouds and at the UV-illuminated edges of dense star-forming clouds, so-called photodissociation regions (PDRs; Hollenbach & Tielens 1997). Sulfur is on the top ten list of most abundant cosmic elements and it is particularly relevant for astrochemistry and star-formation studies. Its low ionization potential (10.4 eV) makes the photoionization of S atoms a dominant source of electrons in molecular gas at intermediate visual extinctions $A_V \approx 2\text{--}4 \text{ mag}$ (Sternberg & Dalgarno 1995; Goicoechea et al. 2009; Fuente et al. 2016).

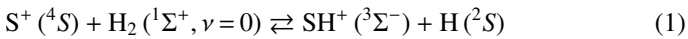
The sulfur abundance, [S/H], in diffuse clouds (Howk et al. 2006) is very close to the [S/H] measured in the solar photosphere ([S/H]_⊙ $\approx 1.4 \times 10^{-5}$; Asplund et al. 2009). Still, the observed abundances of S-bearing molecules in diffuse

and translucent molecular clouds ($n_H \approx 10^2\text{--}10^3 \text{ cm}^{-3}$) make up a very small fraction, <1 %, of the sulfur nuclei (mostly locked as S⁺; Tieftrunk et al. 1994; Turner 1996; Lucas & Liszt 2002; Neufeld et al. 2015). In colder dark clouds and dense cores shielded from stellar UV radiation, most sulfur is expected in molecular form. However, the result of adding the abundances of all detected gas-phase S-bearing molecules is typically a factor of $\sim 10^2\text{--}10^3$ lower than [S/H]_⊙ (e.g., Fuente et al. 2019). Hence, it is historically assumed that sulfur species deplete on grain mantles at cold temperatures and high densities (e.g., Graedel et al. 1982; Millar & Herbst 1990; Agúndez & Wakelam 2013). However, recent chemical models predict that the major sulfur reservoir in dark clouds can be either gas-phase neutral S atoms (Vidal et al. 2017; Navarro-Almida et al. 2020) or organo-sulfur species trapped on grains (Laas & Caselli 2019). Unfortunately, it is difficult to overcome this dichotomy from an observational perspective. In particular, no ice carrier of an

abundant sulfur reservoir other than solid OCS (hereafter s-OCS, with an abundance of $\sim 10^{-8}$ with respect to H nuclei; [Palumbo et al. 1997](#)) has been convincingly identified. Considering the large abundances of water ice (s-H₂O) grain mantles in dense molecular clouds and cold protostellar envelopes (see reviews by [van Dishoeck 2004](#); [Gibb et al. 2004](#); [Dartois 2005](#)), one may also expect hydrogen sulfide (s-H₂S) to be the dominant sulfur reservoir. Indeed, s-H₂S is the most abundant S-bearing ice in comets such as 67P/Churyumov-Gerasimenko ([Calmonte et al. 2016](#)). However, only upper limits to the s-H₂S abundance of $\lesssim 1\%$ relative to water ice have so far been estimated toward a few interstellar sightlines (e.g., [Smith 1991](#); [Jiménez-Escobar & Muñoz Caro 2011](#)). These values imply a maximum s-H₂S ice abundance of several 10^{-6} with respect to H nuclei. Still, this upper limit could be higher if s-H₂S ices are well mixed with s-H₂O and s-CO ices ([Brittain et al. 2020](#)).

The bright rims of molecular clouds illuminated by nearby massive stars are intermediate environments between diffuse and cold dark clouds. Such environments host the transition from ionized S⁺ to neutral atomic S, as well as the gradual formation of S-bearing molecules ([Sternberg & Dalgarno 1995](#)). In one prototypical low-illumination PDR, the edge of the Horsehead nebula, [Goicoechea et al. \(2006\)](#) inferred very modest gas-phase sulfur depletions. In addition, the detection of narrow sulfur radio recombination lines in dark clouds (implying the presence of S⁺; [Pankonin & Walmsley 1978](#)) is an argument against large sulfur depletions in the mildly illuminated surfaces of these clouds. The presence of new S-bearing molecules such as S₂H, the first (and so far only) doubly sulfuretted species detected in a PDR ([Fuente et al. 2017](#)), suggests that the chemical pathways leading to the synthesis of sulfuretted species are not well constrained; and that the list of S-bearing molecules is likely not complete.

Interstellar sulfur chemistry is unusual compared to that of other elements in that none of the simplest species, X = S, S⁺, SH, SH⁺, or H₂S⁺, react exothermically with H₂ ($v=0$) in the initiation reactions $X + H_2 \rightarrow XH + H$ (so-called hydrogen abstraction reactions). Hence, one would expect a slow sulfur chemistry and very low abundances of SH⁺ (sulfanylium) and SH (mercapto) radicals in cold interstellar gas. However, H₂S ([Lucas & Liszt 2002](#)), SH⁺ ([Menten et al. 2011](#); [Godard et al. 2012](#)), and SH ([Neufeld et al. 2012, 2015](#)) have been detected in low-density diffuse clouds ($n_H \lesssim 100 \text{ cm}^{-3}$) through absorption measurements of their ground-state rotational lines¹. In UV-illuminated gas, most sulfur atoms are ionized, but the very high endothermicity of reaction



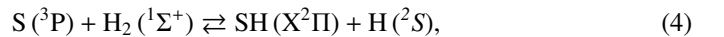
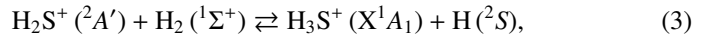
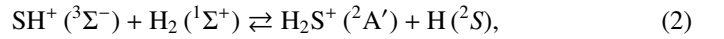
($E/k = 9860 \text{ K}$, e.g., [Zanchet et al. 2013a, 2019](#)) prevents this reaction from being efficient unless the gas is heated to very high temperatures. In diffuse molecular clouds (on average at $T_k \sim 100 \text{ K}$), the formation of SH⁺ and SH only seems possible in the context of local regions of overheated gas subjected to magnetized shocks ([Pineau des Forets et al. 1986](#)) or in dissipative vortices of the interstellar turbulent cascade ([Godard et al. 2012, 2014](#)). In these tiny pockets ($\sim 100 \text{ AU}$ in size), the gas would attain the hot temperatures ($T_k \approx 1000 \text{ K}$) and/or ion-neutral drift needed to overcome the endothermicities of the above hydrogen abstraction reactions (see, e.g., [Neufeld et al. 2015](#)).

¹ SH was first reported by IR spectroscopy toward the circumstellar envelope around the evolved star R Andromedae ([Yamamura et al. 2000](#)).

Dense PDRs ($n_H \approx 10^3\text{--}10^6 \text{ cm}^{-3}$) offer a complementary environment to study the first steps of sulfur chemistry. Because of their higher densities and more quiescent gas, fast shocks or turbulence dissipation do not contribute to the gas heating. Instead, the molecular gas is heated to $T_k \lesssim 500 \text{ K}$ by mechanisms that depend on the flux of far-UV photons (FUV; $E < 13.6 \text{ eV}$). A different perspective of the H₂ (v) reactivity emerges because certain endoergic reactions become exoergic and fast when a significant fraction of the H₂ reagents are radiatively pumped to vibrationally excited states $v \geq 1$ ([Stecher & Williams 1972](#); [Freeman & Williams 1982](#); [Tielens & Hollenbach 1985](#); [Sternberg & Dalgarno 1995](#)). In this case, state-specific reaction rates for H₂ (v, J) are needed to make realistic predictions of the abundance of the product XH ([Agúndez et al. 2010](#); [Zanchet et al. 2013b](#); [Faure et al. 2017](#)). The presence of abundant FUV-pumped H₂ ($v \geq 1$) triggers a nonthermal “hot” chemistry. Indeed, CH⁺ and SH⁺ emission lines have been detected in the Orion Bar PDR ([Nagy et al. 2013](#); [Goicoechea et al. 2017](#)) where H₂ lines up to $v=10$ have been detected as well ([Kaplan et al. 2017](#)).

In this study we present a systematic (observational and modeling) study of the chemistry of S-bearing hydrides in FUV-illuminated gas. We try to answer the question of whether gas-phase reactions of S atoms and SH⁺ molecules with vibrationally excited H₂ can ultimately explain the presence of abundant H₂S, or if grain surface chemistry has to be invoked.

The paper is organized as follows. In Sects. 2 and 3 we report on new observations of H₂³²S, H₂³⁴S, H₂³³S, SH⁺, SH, and H₃S⁺ emission lines toward the Orion Bar. In Sect. 4 we study their excitation and derive their column densities. In Sect. 6 we discuss their abundances in the context of updated PDR models, with emphasis on the role of hydrogen abstraction reactions



photoreactions, and grain surface chemistry. In Sect. 5 we summarize the ab initio quantum calculations we carried out to determine the state-dependent rates of reactions (2) and (4). Details of these calculations are given in Appendices A and B.

2. Observations of S-bearing hydrides

2.1. The Orion Bar

At an adopted distance of $\sim 414 \text{ pc}$, the Orion Bar is an interface of the Orion molecular cloud and the Huygens H II region that surrounds the Trapezium cluster ([Genzel & Stutzki 1989](#); [O'Dell 2001](#); [Bally 2008](#); [Goicoechea et al. 2019, 2020](#); [Pabst et al. 2019, 2020](#)). The Orion Bar is a prototypical strongly illuminated dense PDR. The impinging flux of stellar FUV photons (G_0) is a few 10^4 times the mean interstellar radiation field ([Habing 1968](#)). The Bar is seen nearly edge-on with respect to the FUV illuminating sources, mainly $\theta^1 \text{ Ori C}$, the most massive star in the Trapezium. This favorable orientation allows observers to spatially resolve the H⁺-to-H transition (the ionization front or IF; see, e.g., [Walmsley et al. 2000](#); [Pellegrini et al. 2009](#)) from the H-to-H₂ transition (the dissociation front or DF; see, e.g., [Allers et al. 2005](#); [van der Werf et al. 1996, 2013](#); [Wyrowski et al. 1997](#); [Cuadrado et al. 2019](#)). It also allows one to study the stratification

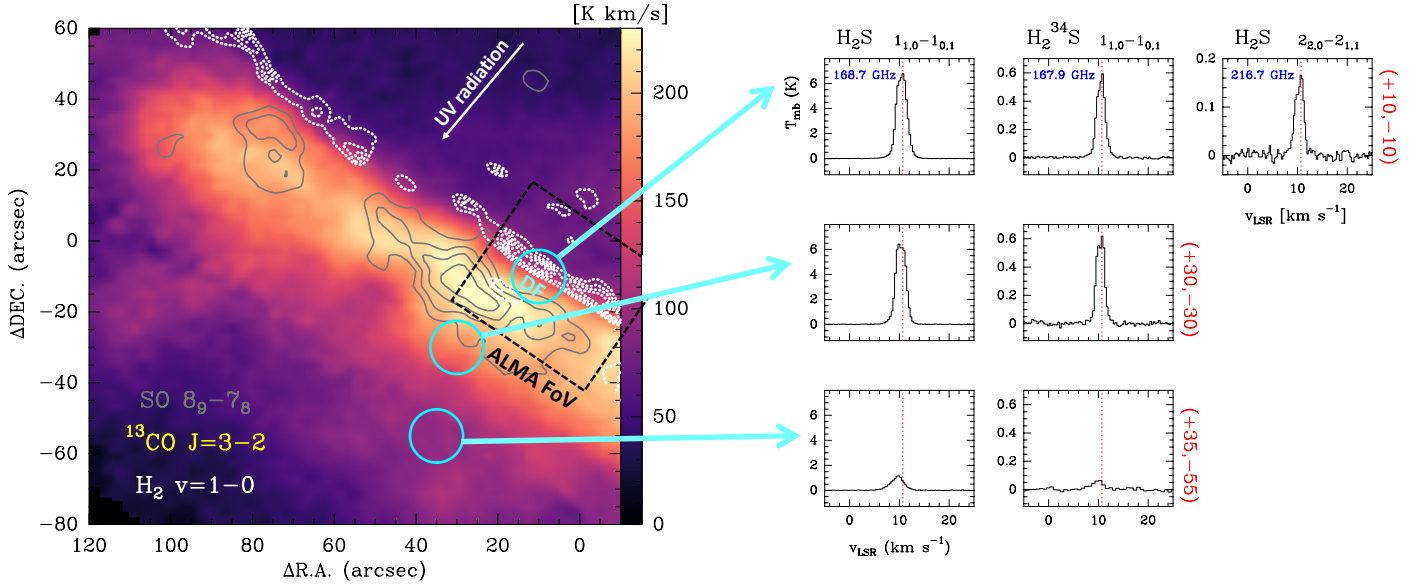


Fig. 1. Overview of the Orion Bar. The $(0'', 0'')$ position corresponds to $\alpha_{2000} = 05^{\text{h}} 35^{\text{m}} 20.1^{\text{s}}$; $\delta_{2000} = -05^{\circ} 25' 07.0''$. *Left panel:* integrated line intensity maps in the $^{13}\text{CO } J=3-2$ (color scale) and $\text{SO } 8_9-7_8$ emission (gray contours; from 6 to 23.5 K km s^{-1} in steps of 2.5 K km s^{-1}) obtained with the IRAM 30m telescope at $8''$ resolution. The white dotted contours delineate the position of the H_2 dissociation front as traced by the infrared $\text{H}_2 v=1-0 S(1)$ line (from 1.5 to $4.0 \times 10^{-4} \text{ erg s}^{-1} \text{ cm}^{-2} \text{ sr}^{-1}$ in steps of $0.5 \times 10^{-4} \text{ erg s}^{-1} \text{ cm}^{-2} \text{ sr}^{-1}$; from Walmsley et al. 2000). The black-dashed rectangle shows the smaller FoV imaged with ALMA (Fig. 3). The DF position has been observed with SOFIA, IRAM 30 m, and *Herschel*. Cyan circles represent the $\sim 15''$ beam at 168 GHz. *Right panel:* H_2S lines detected toward three positions of the Orion Bar.

of different molecular species as a function of cloud depth (i.e., as the flux of FUV photons is attenuated; see, e.g., Tielens et al. 1993; van der Wiel et al. 2009; Habart et al. 2010; Goicoechea et al. 2016; Parikka et al. 2017; Andree-Labsch et al. 2017).

Regarding sulfur², several studies previously reported the detection of S-bearing molecules in the Orion Bar. These include CS, C^{34}S , SO, SO_2 , and H_2S (Hogerheijde et al. 1995; Jansen et al. 1995), SO^+ (Fuente et al. 2003), C^{33}S , HCS^+ , H_2CS , and NS (Leurini et al. 2006), and SH^+ (Nagy et al. 2013). These detections refer to modest angular resolution pointed observations using single-dish telescopes. Higher-angular-resolution interferometric imaging of SH^+ , SO, and SO^+ (Goicoechea et al. 2017) was possible thanks to the Atacama Compact Array (ACA).

2.2. Observations of H_2S isotopologues and H_3S^+

We observed the Orion Bar with the IRAM 30m telescope at Pico Veleta (Spain). We used the EMIR receivers in combination with the Fast Fourier Transform Spectrometer (FTS) backends at 200 kHz resolution (~ 0.4 , ~ 0.3 , and $\sim 0.2 \text{ km s}^{-1}$ at ~ 168 , ~ 217 , and $\sim 293 \text{ GHz}$, respectively). These observations are part of a complete line survey covering the frequency range 80–360 GHz (Cuadrado et al. 2015, 2016, 2017, 2019) and include deep integrations at 168 GHz toward three positions of the PDR located at a distance of $14''$, $40''$, and $65''$ from the IF (see Fig. 1). Their offsets with respect to the IF position at $\alpha_{2000} = 05^{\text{h}} 35^{\text{m}} 20.1^{\text{s}}$, $\delta_{2000} = -05^{\circ} 25' 07.0''$ are $(+10'', -10'')$, $(+30'', -30'')$, and $(+35'', -55'')$. The first position is the DF.

We carried out these observations in the position switching mode taking a distant reference position at $(-600'', 0'')$. The half power beam width (HPBW) at ~ 168 , ~ 217 , and

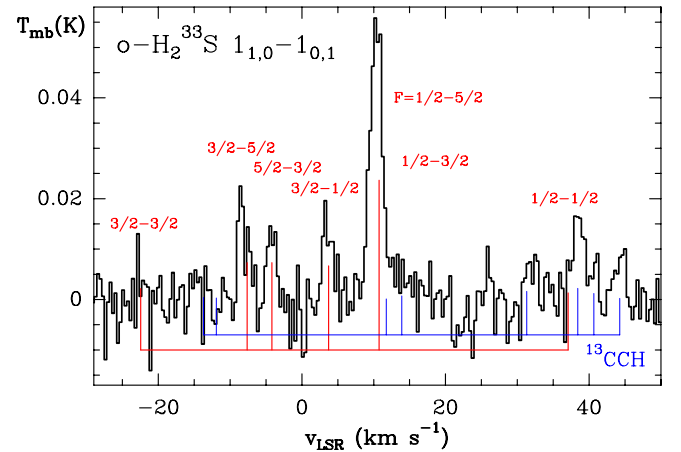


Fig. 2. Detection of H_2^{33}S (at $\sim 168.3 \text{ GHz}$) toward the DF position of the Orion Bar. Red lines indicate hyperfine components. Blue lines show interloping lines from ^{13}CCH . The length of each line is proportional to the transition line strength (taken from the Cologne Database for Molecular Spectroscopy, CDMS; Endres et al. 2016).

$\sim 293 \text{ GHz}$ is $\sim 15''$, $\sim 11''$, and $\sim 8''$, respectively. The latest observations (those at 168 GHz) were performed in March 2020. The data were first calibrated in the antenna temperature scale T_A^* and then converted to the main beam temperature scale, T_{mb} , using $T_{\text{mb}} = T_A^* / \eta_{\text{mb}}$, where η_{mb} is the antenna efficiency ($\eta_{\text{mb}} = 0.74$ at $\sim 168 \text{ GHz}$). We reduced and analyzed the data using the GILDAS software as described in Cuadrado et al. (2015). The typical rms noise of the spectra is ~ 3.5 , 5.3 , and 7.8 mK per velocity channel at ~ 168 , ~ 217 , and $\sim 293 \text{ GHz}$, respectively. Figures 1 and 2 show the detection of $o\text{-H}_2^{33}\text{S } 1_{1,0}-1_{0,1}$ (168.7 GHz), $p\text{-H}_2\text{S } 2_{2,0}-2_{1,1}$ (216.7 GHz), and $o\text{-H}_2^{34}\text{S } 1_{1,0}-1_{0,1}$ lines (167.9 GHz) (see Table E.1 for the line

² Sulfur has four stable isotopes, in decreasing order of abundance: ^{32}S ($I_N = 0$), ^{34}S ($I_N = 0$), ^{33}S ($I_N = 3/2$), and ^{36}S ($I_N = 0$), where I_N is the nuclear spin. The most abundant isotope is here simply referred to as S.

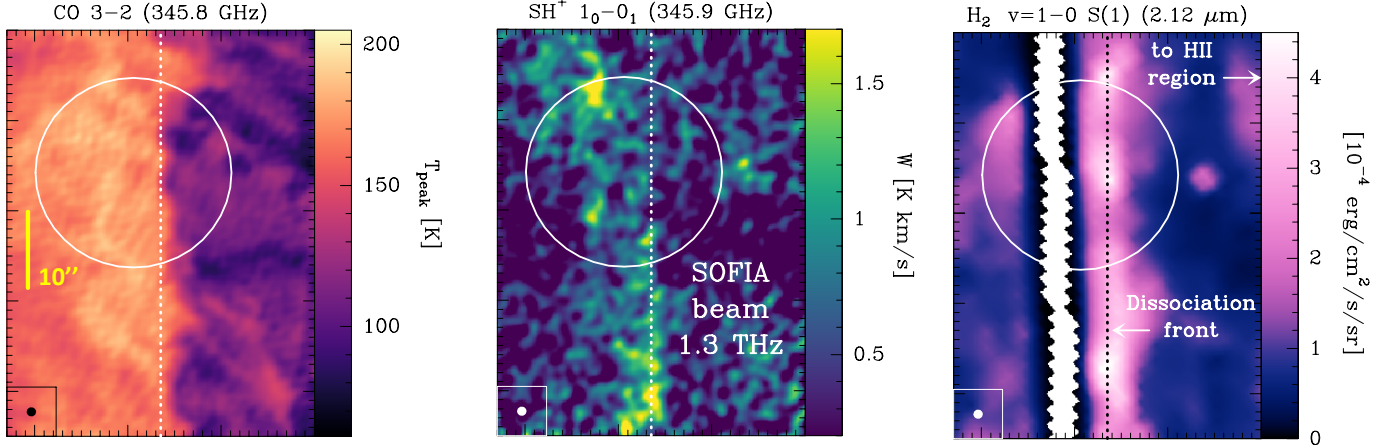


Fig. 3. ALMA 1''-resolution images zooming into the edge of the Orion Bar in ^{12}CO 3–2 (left panel, Goicoechea et al. 2016) and SH^+ 1_0-0_1 $F=1/2-3/2$ line (middle panel, integrated line intensity). The right panel shows the H_2 $v=1-0$ $S(1)$ line (Walmsley et al. 2000). We rotated these images (all showing the same FoV) with respect to Fig. 1 to bring the FUV illuminating direction in the horizontal direction (from the right). The circle shows the DF position targeted with SOFIA in SH (20'' beam) and with the IRAM 30 m telescope in H_2S and H_3S^+ .

parameters), as well as several $o\text{-H}_2^{33}\text{S}$ $1_{1,0}-1_{0,1}$ hyperfine lines (168.3 GHz).

We complemented our dataset with higher frequency H_2S lines detected by the *Herschel* Space Observatory (Nagy et al. 2017) toward the “ CO^+ peak” position (Stoerzer et al. 1995), which is located at only $\sim 4''$ from our DF position (i.e., within the HPBW of these observations). These observations were carried out with the HIFI receiver (de Graauw et al. 2010) at a spectral-resolution of 1.1 MHz (0.7 km s^{-1} at 500 GHz). HIFI’s HPBW range from $\sim 42''$ to $\sim 20''$ in the 500–1000 GHz window (Roelfsema et al. 2012). The list of additional hydrogen sulfide lines detected by *Herschel* includes the $o\text{-H}_2\text{S}$ $2_{2,1}-2_{1,2}$ (505.5 GHz), $2_{1,2}-1_{0,1}$ (736.0 GHz), and $3_{0,3}-2_{1,2}$ (993.1 GHz), as well as the $p\text{-H}_2\text{S}$ $2_{0,2}-1_{1,1}$ (687.3 GHz) line. We used the line intensities, in the T_{mb} scale, shown in Table A.1 of Nagy et al. (2017).

In order to get a global view of the Orion Bar, we also obtained $2.5' \times 2.5'$ maps of the region observed by us with the IRAM 30 m telescope using the 330 GHz EMIR receiver and the FTS backend at 200 kHz spectral-resolution ($\sim 0.2 \text{ km s}^{-1}$). On-the-fly (OTF) scans were obtained along and perpendicular to the Bar. The resulting spectra were gridded to a data cube through convolution with a Gaussian kernel providing a final resolution of $\sim 8''$. The total integration time was ~ 6 h. The achieved rms noise is $\sim 1 \text{ K}$ per resolution channel. Figure 1 shows the spatial distribution of the ^{13}CO $J=3-2$ (330.5 GHz) and SO 8_9-7_8 (346.5 GHz) integrated line intensities.

2.3. ALMA imaging of Orion Bar edge in SH^+ emission

We carried out mosaics of a small field of the Orion Bar using twenty-seven ALMA 12 m antennas in band 7 (at ~ 346 GHz). These unpublished observations belong to project 2012.1.00352.S (PI: J. R. Goicoechea) and consisted of a 27-pointing mosaic centered at $\alpha(2000)=5^{\text{h}}35^{\text{m}}20.6^{\text{s}}$; $\delta(2000)=-05^{\circ}25'20''$. The total field-of-view (FoV) is $58'' \times 52''$ (shown in Fig. 1). The two hyperfine line components of the SH^+ $N_J=1_0-0_1$ transition were observed with correlators providing ~ 500 kHz resolution (0.4 km s^{-1}) over a 937.5 MHz bandwidth. The total observation time with the ALMA 12 m array was ~ 2 h. In order to recover the large-scale extended emission filtered out by the interferometer, we used deep and

fully sampled single-dish maps, obtained with the total-power (TP) antennas at $19''$ resolution, as zero- and short-spacings. Data calibration procedures and image synthesis steps are described in Goicoechea et al. (2016). The synthesized beam is $\sim 1''$. This is a factor of ~ 4 better than previous interferometric SH^+ observations (Goicoechea et al. 2017). Figure 3 shows the resulting image of the SH^+ 1_0-0_1 $F=1/2-3/2$ hyperfine emission line at 345.944 GHz. We rotated this image 37.5° clockwise to bring the FUV illumination in the horizontal direction. The typical rms noise of the final cube is $\sim 80 \text{ mK}$ per velocity channel and $1''$ -beam. As expected from their Einstein coefficients, the other $F=1/2-1/2$ hyperfine line component at 345.858 GHz is a factor of ~ 2 fainter (see Table E.2) and the resulting image has low signal-to-noise (S/N).

We complemented the SH^+ dataset with the higher frequency lines observed by HIFI (Nagy et al. 2013, 2017) at ~ 526 and ~ 683 GHz (upper limit). These pointed observations have HPBW of $\sim 41''$ and $\sim 32''$ respectively, thus they do not spatially resolve the SH^+ emission. To determine their beam coupling factors (f_b), we smoothed the bigger $4''$ -resolution ACA + TP SH^+ image shown in Goicoechea et al. (2017) to the different HIFI’s HPBW. We obtain $f_b \simeq 0.4$ at ~ 526 GHz and $f_b \simeq 0.6$ at ~ 683 GHz. The corrected intensities are computed as $W_{\text{corr}} = W_{\text{HIFI}} / f_b$. These correction factors are only a factor of $\lesssim 2$ lower than simply assuming uniform SH^+ emission from a $10''$ width filament.

2.4. SOFIA/GREAT search for SH emission

We finally used the GREAT receiver (Heyminck et al. 2012) on board the Stratospheric Observatory For Infrared Astronomy (SOFIA; Young et al. 2012) to search for the lowest-energy rotational lines of SH ($^2\Pi_{3/2}$ $J=3/2-1/2$) at 1382.910 and 1383.241 GHz (e.g., Klisch et al. 1996; Martin-Drumel et al. 2012). These lines lie in a frequency gap that *Herschel*/HIFI could not observe from space. These SOFIA observations belong to project 07_0115 (PI: J. R. Goicoechea). The SH lines were searched on the lower side band of 4GREAT band 3. We employed the 4GREAT/HFA frontends and 4GFFT spectrometers as backends. The HPBW of SOFIA at 1.3 THz is $\sim 20''$, thus comparable with IRAM 30 m/EMIR and *Herschel*/HIFI observations. We also employed the total power mode with a reference

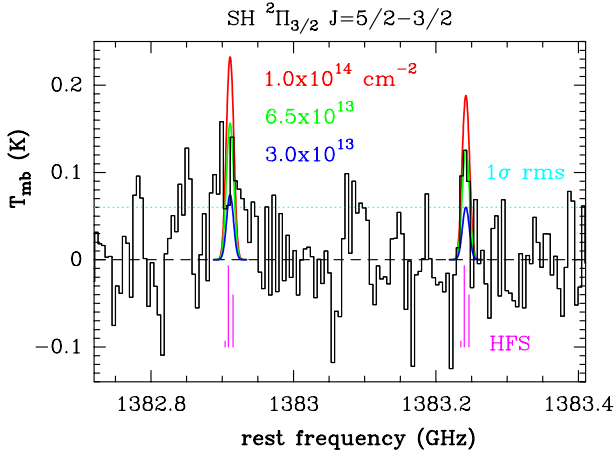


Fig. 4. Search for the SH $^2\Pi_{3/2} J=5/2-3/2$ doublet (at ~ 1383 GHz) toward the DF position with SOFIA/GREAT. Vertical magenta lines indicate the position of hyperfine splittings taken from CDMS.

position at $(-600'', 0'')$. The original plan was to observe during two flights in November 2019 but due to bad weather conditions, only ~ 70 min of observations were carried out in a single flight.

After calibration, data reduction included: removal of a first order spectral baseline, dropping scans with problematic receiver response, rms weighted average of the spectral scans, and calibration to T_{mb} intensity scale ($\eta_{\text{mb}} = 0.71$). The final spectrum, smoothed to a velocity-resolution of 1 km s^{-1} has a rms noise of $\sim 50 \text{ mK}$ (shown in Fig. 4). Two emission peaks are seen at the frequencies of the Λ -doublet lines. Unfortunately, the achieved rms is not enough to assure the unambiguous detection of each component of the doublet. Although the stacked spectrum does display a single line (suggesting a tentative detection) the resulting line-width ($\Delta v \approx 7 \text{ km s}^{-1}$) is a factor of ~ 3 broader than expected in the Orion Bar (see Table E.3). Hence, this spectrum provides stringent upper limits to the SH column density but deeper integrations would be needed to confirm the detection.

3. Observational results

3.1. H_2^{32}S , H_2^{34}S , and H_2^{33}S across the PDR

Figure 1 shows an expanded view of the Orion Bar in the $^{13}\text{CO} (J=3-2)$ emission. FUV radiation from the Trapezium stars comes from the upper-right corner of the image. The FUV radiation field is attenuated in the direction perpendicular to the Bar. The infrared $\text{H}_2 v=1-0 S(1)$ line emission (white contours) delineates the position of the H-to- H_2 transition, the DF. Many molecular species, such as SO, specifically emit from deeper inside the PDR where the flux of FUV photons has considerably decreased. In contrast, H_2S , and even its isotopologue H_2^{34}S , show bright $1_{1,0}-1_{0,1}$ line emission toward the DF (right panels in Fig. 1; see also Jansen et al. 1995). Rotationally excited H_2S lines have been also detected toward this position (Nagy et al. 2017), implying the presence of warm H_2S close to the irradiated cloud surface (i.e., at relatively low extinctions). The presence of moderately large H_2S column densities in the PDR is also demonstrated by the unexpected detection of the rare isotopologue H_2^{33}S toward the DF (at the correct LSR velocity of the PDR: $v_{\text{LSR}} \approx 10.5 \text{ km s}^{-1}$). Figure 2 shows the $\text{H}_2^{33}\text{S} 1_{1,0}-1_{0,1}$ line and its hyperfine splittings (produced by the ^{33}S nuclear spin). To our knowledge, H_2^{33}S lines had only been reported toward the hot cores in Sgr B2 and Orion KL before (Crockett et al. 2014).

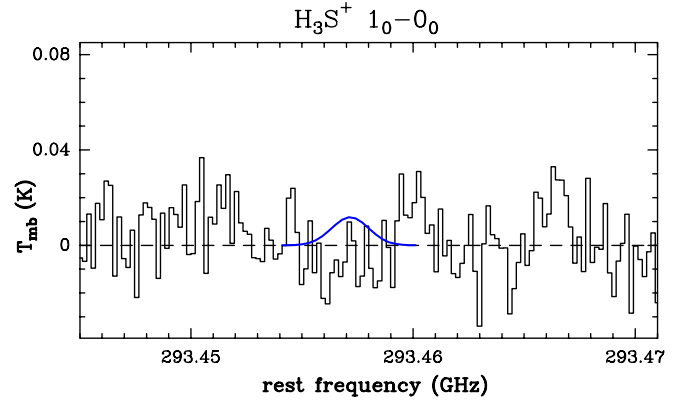


Fig. 5. Search for H_3S^+ toward the Orion Bar with the IRAM 30 m telescope. The blue curve shows the expected position of the line.

The observed $o\text{-H}_2\text{S}/o\text{-H}_2^{34}\text{S} 1_{1,0}-1_{0,1}$ line intensity ratio toward the DF is 15 ± 2 , below the solar isotopic ratio of $^{32}\text{S}/^{34}\text{S} = 23$ (e.g., Anders & Grevesse 1989). The observed ratio thus implies optically thick $o\text{-H}_2\text{S}$ line emission at $\sim 168 \text{ GHz}$. However, the observed $o\text{-H}_2^{34}\text{S}/o\text{-H}_2^{33}\text{S} 1_{1,0}-1_{0,1}$ intensity ratio is 6 ± 1 , thus compatible with the solar isotopic ratio ($^{34}\text{S}/^{33}\text{S} = 5.5$) and with H_2^{34}S and H_2^{33}S optically thin emission.

3.2. SH^+ emission from the PDR edge

Figure 3 zooms into a small field of the Bar edge. The ALMA image of the CO $J=3-2$ line peak temperature was first presented by Goicoechea et al. (2016). Because the CO $J=3-2$ emission is nearly thermalized and optically thick from the DF to the molecular cloud interior, the line peak temperature scale (T_{peak}) is a good proxy of the gas temperature ($T_{\text{k}} \approx T_{\text{ex}} \approx T_{\text{peak}}$). The CO image implies small temperature variations around $T_{\text{k}} \approx 200 \text{ K}$. The middle panel in Fig. 3 shows the ALMA image of the $\text{SH}^+ N_J = 1_0-0_1 F = 1/2-3/2$ hyperfine line at 345.944 GHz . Compared to CO, the SH^+ emission follows the edge of the molecular PDR, akin to a filament of $\sim 10''$ width (for the spatial distribution of other molecular ions, see, Goicoechea et al. 2017). The SH^+ emission shows localized small-scale emission peaks (density or column density enhancements) that match, or are very close to, the vibrationally excited $\text{H}_2 (v=1-0)$ emission (Fig. 3). We note that while some $\text{H}_2 (v=1-0)$ emission peaks likely coincide with gas density enhancements (e.g., Burton et al. 1990), the region also shows extended emission from FUV-pumped $\text{H}_2 (v=2-1)$ (van der Werf et al. 1996) that does not necessarily coincide with the $\text{H}_2 (v=1-0)$ emission peaks.

3.3. Search for SH, H_3S^+ , and $\text{H}_2\text{S} v_2 = 1$ emission

We used SOFIA/GREAT to search for SH $^2\Pi_{3/2} J=5/2-3/2$ lines toward the DF (Fig. 4). This would have been the first time that interstellar SH rotational lines were seen in emission. Unfortunately, the achieved rms of the observation does not allow a definitive confirmation of these lines, so here we will only discuss upper limits to the SH column density. The red, green, and blue curves in Fig. 4 show radiative transfer models for $n_{\text{H}} = 10^6 \text{ cm}^{-3}$, $T_{\text{k}} = 200 \text{ K}$, and different SH column densities (see Sect. 4 for more details).

Our IRAM 30 m observations toward the DF neither resulted in a detection of H_3S^+ , a key gas-phase precursor of H_2S . The $\sim 293.4 \text{ GHz}$ spectrum around the targeted $\text{H}_3\text{S}^+ 1_0-0_0$ line is

shown in Fig. 5. Again, the achieved low rms allows us to provide a sensitive upper limit to the H_3S^+ column density. This results in $N(\text{H}_3\text{S}^+) = (5.5\text{--}7.5) \times 10^{10} \text{ cm}^{-2}$ (5σ) assuming an excitation temperature range $T_{\text{ex}} = 10\text{--}30 \text{ K}$ and extended emission. Given the bright H_2S emission close to the edge of the Orion Bar, and because H_2S formation at the DF might be driven by very exoergic processes, we also searched for the $1_{1,0}\text{--}1_{0,1}$ line of vibrationally excited H_2S (in the bending mode ν_2). The frequency of this line lies at $\sim 181.4 \text{ GHz}$ (Azzam et al. 2013), thus at the end of our 2 mm-band observations of the DF (rms $\approx 16 \text{ mK}$). However, we do not detect this line either.

4. Coupled nonlocal excitation and chemistry

In this section we study the rotational excitation of the observed S-bearing hydrides³. We determine the SH^+ , SH (upper limit), and H_2S column densities in the Orion Bar, and the “average” gas physical conditions in the sense that we search for the combination of single T_k , n_{H} , and N that better reproduces the observed line intensities (so-called “single-slab” approach). In Sect. 6 we expand these excitation models to multi-slab calculations that take into account the expected steep gradients in a PDR.

In the ISM, rotationally excited levels are typically populated by inelastic collisions. However, the lifetime of very reactive molecules can be so short that the details of their formation and destruction need to be taken into account when determining how these levels are actually populated (Black 1998). Reactive collisions (collisions that lead to a reaction and thus to molecule destruction) influence the excitation of these species when their timescales become comparable to those of nonreactive collisions. The lifetime of reactive molecular ions observed in PDRs (e.g., Fuente et al. 2003; Nagy et al. 2013; van der Tak et al. 2013; Goicoechea et al. 2017, 2019) can be so short that they do not get thermalized by nonreactive collisions or by absorption of the background radiation field (Black 1998). In these cases, a proper treatment of the molecule excitation requires including chemical formation and destruction rates in the statistical equilibrium equations ($dn_i/dt = 0$) that determine the level populations:

$$\sum_{j>i} n_j A_{ji} + \sum_{j\neq i} n_j (B_{ji} \bar{J}_{ji} + C_{ji}) + F_i \quad (5)$$

$$= n_i \left(\sum_{j<i} A_{ij} + \sum_{j\neq i} (B_{ij} \bar{J}_{ij} + C_{ij}) + D_i \right), \quad (6)$$

where $n_i [\text{cm}^{-3}]$ is the population of rotational level i , A_{ij} and B_{ij} are the Einstein coefficients for spontaneous and induced emission, $C_{ij} [\text{s}^{-1}]$ is the rate of inelastic collisions⁴ ($C_{ij} = \sum_k \gamma_{ij,k} n_k$, where $\gamma_{ij,k}(T) [\text{cm}^3 \text{s}^{-1}]$ are the collisional rate coefficients and k stands for H_2 , H , and e^-), and \bar{J}_{ij} is the mean intensity of the total radiation field over the line profile. In these equations, $n_i D_i$ is the destruction rate per unit volume of the molecule in level i , and F_i its formation rate per unit volume (both in $\text{cm}^{-3} \text{s}^{-1}$). When state-to-state formation rates are not available, and assuming that the destruction rate is the same in every level ($D_i = D$),

³ Readers interested only in the chemistry of these species and in depth-dependent PDR models could directly jump to Sect. 6.

⁴ We use the following inelastic collision rate coefficients γ_{ij} :

- $\text{SH}^+ - e^-$, including hyperfine splittings (Hamilton et al. 2018).
- $\text{SH}^+ - o\text{-H}_2$ and $p\text{-H}_2$, including hyperfine splittings (Dagdigan 2019a).
- $\text{SH}^+ - \text{H}$, including hyperfine splittings (Lique et al. 2020).
- $o\text{-H}_2\text{S}$ and $p\text{-H}_2\text{S}$ with $o\text{-H}_2$ and $p\text{-H}_2$ (Dagdigan 2020).
- $\text{SH} - \text{He}$, including fine-structure splittings (Kłos et al. 2009).

one can use the total destruction rate $D [\text{s}^{-1}] (= \sum_k n_k k_k(T) + \text{photodestruction rate, where } k_k [\text{cm}^3 \text{s}^{-1}] \text{ is the state-averaged rate of the two-body chemical reaction with species } k)$ and consider that the level populations of the nascent molecule follow a Boltzmann distribution at an effective formation temperature T_{form} :

$$F_i = F g_i e^{-E_i/kT_{\text{form}}} / Q(T_{\text{form}}). \quad (7)$$

In this formalism, $F [\text{cm}^{-3} \text{s}^{-1}]$ is the state-averaged formation rate per unit volume, g_i the degeneracy of level i , and $Q(T_{\text{form}})$ is the partition function at T_{form} (van der Tak et al. 2007).

This “formation pumping” formalism has been previously implemented in large velocity gradient codes to treat, for example, the local excitation of the very reactive ion CH^+ (Nagy et al. 2013; Godard & Cernicharo 2013; Zanchet et al. 2013b; Faure et al. 2017). However, interstellar clouds are inhomogeneous and gas velocity gradients are typically modest at small spatial scales. This means that line photons can be absorbed and reemitted several times before leaving the cloud. Here we implemented this formalism in a Monte Carlo code that explicitly models the nonlocal behavior of the excitation and radiative transfer problem (see Appendix of Goicoechea et al. 2006).

Although radiative pumping by dust continuum photons does not generally dominate in PDRs, for completeness we also included radiative excitation by a modified blackbody at a dust temperature of $\sim 50 \text{ K}$ and a dust opacity $\tau_{\lambda} = 0.03 (150/\lambda[\mu\text{m}])^{1.6}$ (which reproduces the observed intensity and wavelength dependence of the dust emission in the Bar; Arab et al. 2012). The molecular gas fraction, $f(\text{H}_2) = 2n(\text{H}_2)/n_{\text{H}}$, is set to $2/3$, where $n_{\text{H}} = n(\text{H}) + 2n(\text{H}_2)$ is the total density of H nuclei. This choice is appropriate for the dissociation front and implies $n(\text{H}_2) = n(\text{H})$. As most electrons in the DF come from the ionization of carbon atoms, the electron density n_e is set to $n_e \approx n(\text{C}^+) = 1.4 \times 10^{-4} n_{\text{H}}$ (e.g., Cuadrado et al. 2019). For the inelastic collisions with $o\text{-H}_2$ and $p\text{-H}_2$, we assumed that the H_2 ortho-to-para (OTP) ratio is thermalized to the gas temperature.

4.1. SH^+ excitation and column density

We start by assuming that the main destruction pathway of SH^+ are reactions with H atoms and recombinations with electrons (see Sect. 6.1). Hence, the SH^+ destruction rate is $D \approx n_e k_e(T) + n(\text{H}) k_{\text{H}}(T)$ (see Table 1 for the relevant chemical destruction rates). For $T_k = T_e = 200 \text{ K}$ and $n_{\text{H}} = 10^6 \text{ cm}^{-3}$ (e.g., Goicoechea et al. 2016) this implies $D \approx 10^{-4} \text{ s}^{-1}$ (i.e., the lifetime of an SH^+ molecule in the Bar is less than 3 h). At these temperatures and densities, D is about ten times smaller than the rate of radiative and inelastic collisional transitions that depopulate the lowest-energy rotational levels of SH^+ . Hence, formation pumping does not significantly alter the excitation of the observed SH^+ lines, but it does influence the population of higher-energy levels. Formation pumping effects have been readily seen in CH^+ because this species is more reactive⁵ and its rotationally excited levels lie at higher-energy (i.e., their inelastic collision pumping rates are slower, e.g., Zanchet et al. 2013b).

Figure 6 shows results of several models: without formation pumping (dotted curves for model “ $F = D = 0$ ”), adding formation pumping with SH^+ destruction by H and e^- (continuous curves for model “ F, D ”), and using a factor of ten higher SH^+

⁵ CH^+ is more reactive than SH^+ because CH^+ does react with $\text{H}_2(v=0)$ exothermically producing CH_2^+ at $k = 1.2 \times 10^{-9} \text{ cm}^3 \text{s}^{-1}$ (Anicich 2003) and also because reaction of CH^+ with H is faster, $k = 7.5 \times 10^{-10} \text{ cm}^3 \text{s}^{-1}$.

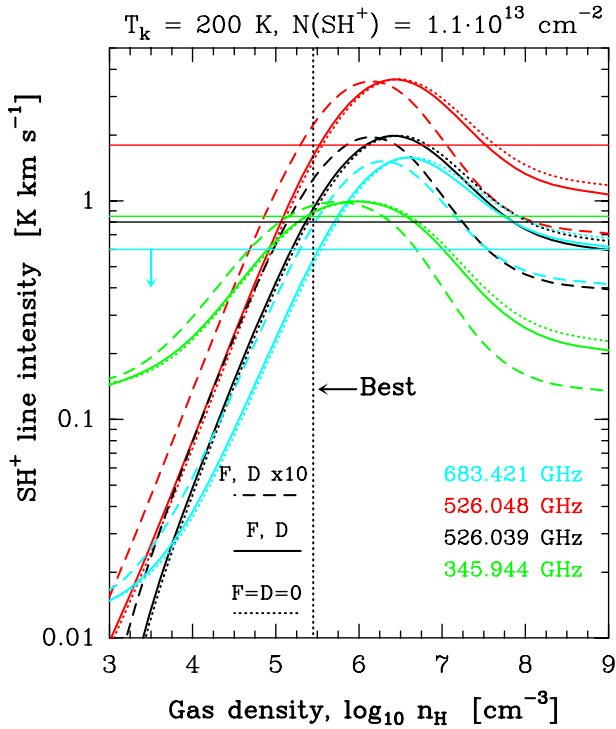


Fig. 6. Non-LTE excitation models of SH^+ . The horizontal lines mark the observed line intensities in the Orion Bar. Dotted curves are for a standard model ($F = D = 0$). Continuous curves are for a model that includes chemical destruction by H atoms and e^- (model F, D). Dashed lines are for a model in which destruction rates are multiplied by ten (model $F, D \times 10$). The vertical black line marks the best model.

destruction rates (simulating a dominant role of SH^+ photodissociation or destruction by reactions with vibrationally excited H_2 ; dashed curves for model “ $F, D \times 10$ ”). Since the formation of SH^+ is driven by reaction (1) when H_2 molecules are in $v \geq 2$, here we adopted $T_{\text{form}} \simeq E(v=2, J=0)/k - 9860 \text{ K} \approx 2000 \text{ K}$. Because these are constant column density $N(\text{SH}^+)$ excitation and radiative transfer models, we used a normalized formation rate $F = \sum F_i$ that assumes steady-state SH^+ abundances consistent with the varying gas density in each model. That is, $F = \sum F_i = x(\text{SH}^+) n_{\text{H}} D [\text{cm}^{-3} \text{s}^{-1}]$, where x refers to the abundance with respect to H nuclei.

The detected SH^+ rotational lines connect the fine-structure levels $N_J = 1_0-0_1$ (345 GHz) and 1_2-0_1 (526 GHz). Upper limits also exist for the 1_1-0_1 (683 GHz) lines. SH^+ critical densities ($n_{\text{cr}} = A_{ij}/\gamma_{ij}$) for inelastic collisions with H or H_2 are of the same order and equal to several 10^6 cm^{-3} . As for many molecular ions (e.g., Desrousseaux et al. 2021), SH^+-H_2 (and SH^+-H) inelastic collisional rate coefficients⁴ are large ($\gamma_{ij} \gtrsim 10^{-10} \text{ cm}^3 \text{s}^{-1}$). Thus, collisions with H (at low A_V) and H_2 (at higher A_V) generally dominate over collisions with electrons (γ_{ij} of a few $10^{-7} \text{ cm}^3 \text{s}^{-1}$). At low densities (meaning $n_{\text{H}} < n_{\text{cr}}$) formation pumping increases the population of the higher-energy levels (and their T_{ex}), but there are only minor effects in the low-energy submillimeter lines. At high densities, $n_{\text{H}} > 10^7 \text{ cm}^{-3}$, formation pumping with $T_{\text{form}} = 2000 \text{ K}$ produces lower intensities in these lines because the lowest-energy levels ($E_u/k < T_k < T_{\text{form}}$) are less populated.

The best fit to the observed lines in model F, D is for $N(\text{SH}^+) \simeq 1.1 \times 10^{13} \text{ cm}^{-2}$, $n_{\text{H}} \simeq 3 \times 10^5 \text{ cm}^{-3}$, and $T_k \simeq 200 \text{ K}$. This is shown by the vertical dotted line in Fig. 6. This model is consistent with the upper limit intensity of the 683 GHz

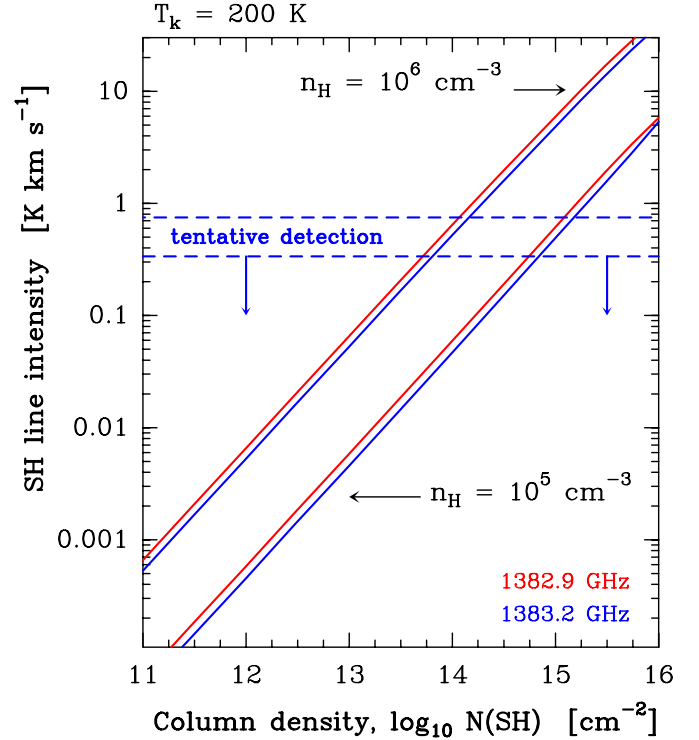


Fig. 7. Non-LTE excitation models of SH emission lines targeted with SOFIA/GREAT. Horizontal dashed lines refer to observational limits, assuming extended emission (lower intensities) and for a $10''$ width emission filament at the PDR surface (higher intensities).

line (Nagy et al. 2013). In this comparison, and following the morphology of the SH^+ emission revealed by ALMA (Fig. 3), we corrected the line intensities of the SH^+ lines detected by *Herschel*/HIFI with the beam coupling factors discussed in Sect. 2.3. The observed $1_2-0_1/1_0-0_1$ line ratio ($R = W(526.048)/W(345.944) \simeq 2$) is sensitive to the gas density. In these models, R is 1.1 for $n_{\text{H}} = 10^5 \text{ cm}^{-3}$ and 3.0 for $n_{\text{H}} = 10^6 \text{ cm}^{-3}$. We note that n_{H} could be lower if SH^+ formation/destruction rates were faster, as in the $F, D \times 10$ model. This could happen if SH^+ photodissociation or destruction reactions with $\text{H}_2(v \geq 2)$ were faster than reactions of SH^+ with H atoms or with electrons. In Sect. 6 we show that this is not the case.

4.2. SH excitation and column density

SH is a $^2\Pi$ open-shell radical with fine-structure, Λ -doubling, and hyperfine splittings (e.g., Martin-Drumel et al. 2012). However, the frequency separation of the $\text{SH } ^2\Pi_{3/2} J=5/2-3/2$ hyperfine components is too small to be spectrally resolved in observations of the Orion Bar (see Fig. 4). The available rate coefficients for inelastic collisions of SH with helium atoms do not resolve the hyperfine splittings. Hence, we first determined line frequencies, level degeneracies, and Einstein coefficients of an SH molecule without hyperfine structure. To do this, we took the complete set of hyperfine levels tabulated in CDMS. Lacking specific inelastic collision rate coefficients, we scaled the available $\text{SH}-\text{He}$ rates of Kłos et al. (2009) by the square root of the reduced mass ratios and estimated the $\text{SH}-\text{H}$ and $\text{SH}-\text{H}_2$ collisional rates.

The scaled rate coefficients are about an order of magnitude smaller than those of SH^+ . However, the chemical destruction rate of SH at the PDR edge (reactions with H, photodissociation,

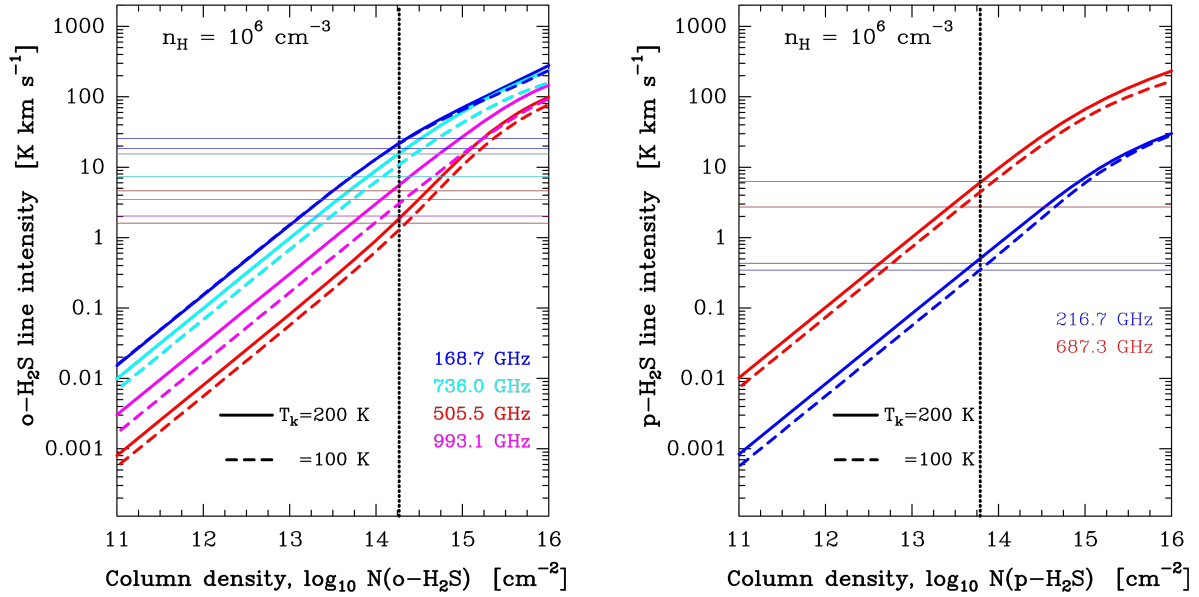


Fig. 8. Non-LTE excitation models for o -H₂S and p -H₂S. Thin horizontal lines show the observed intensities assuming either extended emission (lower limit) or emission that fills the 15'' beam at 168.7 GHz. The vertical line marks the best model, resulting in an OTP ratio of 2.9 ± 0.3 .

and photoionization, see Sect. 6.1) is also slower (we take the rates of SH–H reactive collisions from Zanchet et al. 2019). We determine $D \approx 3 \times 10^{-6} \text{ s}^{-1}$ for $n_{\text{H}} = 10^6 \text{ cm}^{-3}$, $T_{\text{k}} = 200 \text{ K}$, and $A_{\text{V}} \approx 0.7 \text{ mag}$. Models in Fig. 7 include these chemical rates for $T_{\text{form}} = T_{\text{k}}$ (a lower limit to the unknown formation temperature). Formation pumping enhances the intensity of the $^2\Pi_{3/2} J = 5/2-3/2$ ground-state lines by a few percent only.

To estimate the SH column density in the Orion Bar we compare with the upper limit intensities of the SH lines targeted by SOFIA. If SH and SH⁺ arise from roughly the same gas at similar physical conditions ($n_{\text{H}} \approx 10^6 \text{ cm}^{-3}$ and $T_{\text{k}} \approx 200 \text{ K}$) the best model column density is for $N(\text{SH}) \leq (0.6-1.6) \times 10^{14} \text{ cm}^{-2}$. If densities were lower, around $n_{\text{H}} \approx 10^5 \text{ cm}^{-3}$, the upper limit $N(\text{SH})$ column densities will be a factor ten higher.

4.3. H₂S excitation and column density

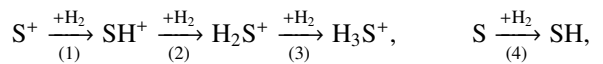
H₂S has a X^2A ground electronic state and two nuclear spin symmetries that we treat separately, o -H₂S and p -H₂S. Previous studies of the H₂S line excitation have used collisional rates coefficients scaled from those of the H₂O–H₂ system. Dagdigan (2020) recently carried out specific calculations of the cross sections of o -H₂S and p -H₂S inelastic collisions with o -H₂ and p -H₂ at different temperatures. The behavior of the new and the scaled rates is different and it depends on the H₂ OTP ratio (e.g., on gas temperature) because the collisional cross sections are different for o -H₂–H₂S and p -H₂–H₂S systems. At the warm temperatures of the PDR, collisions with o -H₂ dominate, resulting in rate coefficients for the $\sim 168 \text{ GHz}$ o -H₂S line that are a factor up to ~ 2.5 smaller than those scaled from H₂O–H₂.

H₂S is not a reactive molecule. At the edge of the PDR its destruction is driven by photodissociation. We determine that the radiative and collisional pumping rates are typically a factor of ~ 100 higher than $D \approx 2 \times 10^{-6} \text{ s}^{-1}$ (for $n_{\text{H}} = 10^6 \text{ cm}^{-3}$, $T_{\text{k}} = 200 \text{ K}$, $G_0 \approx 10^4$, and $A_{\text{V}} \approx 0.7 \text{ mag}$). Figure 8 shows non-LTE o -H₂S and p -H₂S excitation and radiative transfer models. As H₂S may have its abundance peak deeper inside the PDR and display more extended emission than SH⁺ (e.g., Sternberg & Dalgarno 1995), we show results for $T_{\text{k}} = 200$

and 100 K. When comparing with the observed line intensities, we considered either emission that fills all beams, or a correction that assumes that the H₂S emission only fills the 15'' beam of the IRAM 30 m telescope at 168 GHz. The vertical dotted lines in Fig. 8 show the best model, $N(\text{H}_2\text{S}) = N(o\text{-H}_2\text{S}) + N(p\text{-H}_2\text{S}) = 2.5 \times 10^{14} \text{ cm}^{-2}$, with an OTP ratio of 2.9 ± 0.3 , thus consistent with the high-temperature statistical ratio of 3/1 (see discussion at the end of Sect. 6.4). Models with lower densities, $n_{\text{H}} \approx 10^5 \text{ cm}^{-3}$, show worse agreement, and would translate into even higher $N(\text{H}_2\text{S})$ of $\geq 10^{15} \text{ cm}^{-2}$. In either case, these calculations imply large columns of warm H₂S toward the PDR. They result in a limit to the SH to H₂S column density ratio of $\leq 0.2-0.6$. This upper limit is already lower than the $N(\text{SH})/N(\text{H}_2\text{S}) = 1.1-3.0$ ratios observed in diffuse clouds (Neufeld et al. 2015). This difference suggests an enhanced H₂S formation mechanism in FUV-illuminated dense gas.

5. New results on sulfur-hydride reactions

In this section we summarize the ab initio quantum calculations we carried out to determine the vibrationally-state-dependent rates of gas-phase reactions of H₂($v > 0$) with several S-bearing species. We recall that all hydrogen abstraction reactions,



are very endoergic for H₂($v=0$), with endothermicities in Kelvin units that are significantly higher than T_{k} even in PDRs. This is markedly different to O⁺ chemistry, for which all hydrogen abstraction reactions leading to H₃O⁺ are exothermic and fast (Gerin et al. 2010; Neufeld et al. 2010; Hollenbach et al. 2012).

The endothermicity of reactions involving H_nS⁺ ions decreases as the number of hydrogen atoms increases. The potential energy surfaces (PES) of these reactions possess shallow wells at the entrance and products channels (shown in Fig. 9). In addition, these PESs show saddle points between the energy walls of reactants and products whose heights increase with the number of H atoms. For reaction (2), the saddle point has an energy of 0.6 eV ($\approx 7000 \text{ K}$) and is slightly below the energy of

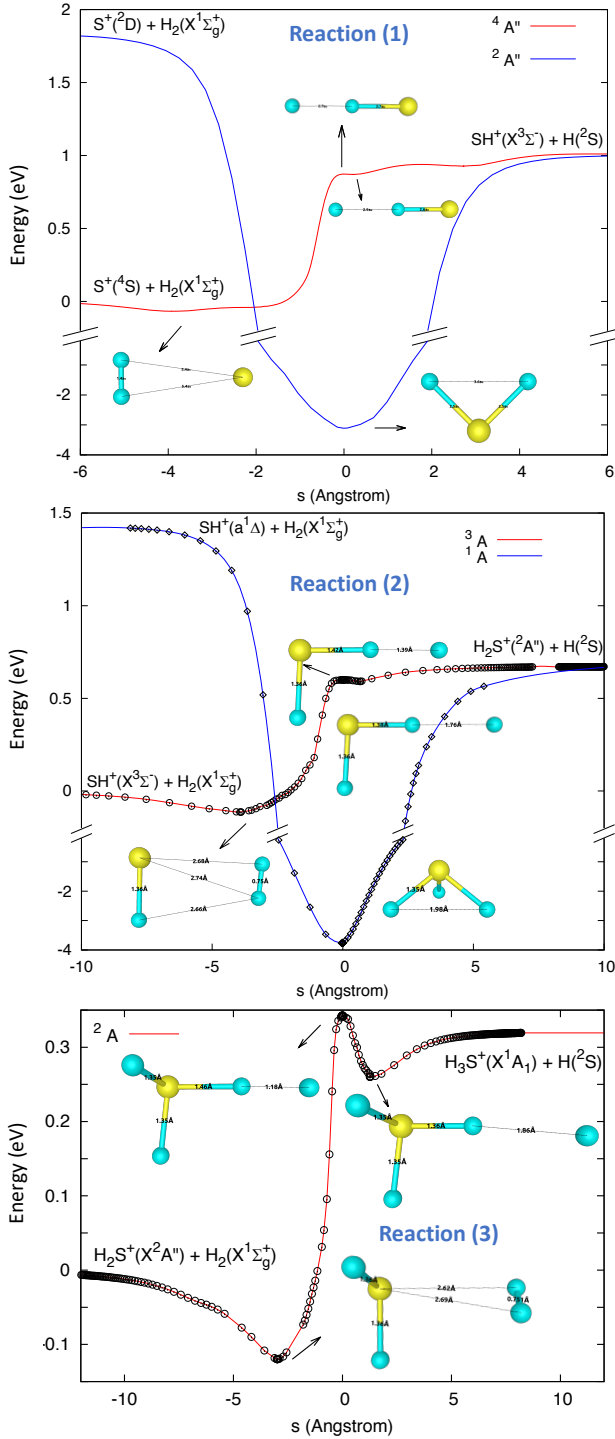


Fig. 9. Minimum energy paths for reactions (1), (2), and (3). Points correspond to RCCSD(T)-F12a calculations and lines to fits (Appendix A). The reaction coordinate, s , is defined independently for each path. The geometries of each species at $s=0$ are different.

the products. However, for reaction (3), the saddle point is above the energy of the products and is a reaction barrier. These saddle points act as a bottleneck in the gas-phase hydrogenation of S^+ .

If one considers the state dependent reactivity of vibrationally excited H_2 , the formation of SH^+ through reaction (1) becomes exoergic⁶ when $v \geq 2$ (Zanchet et al. 2019). The

Table 1. Relevant rate coefficients from a fit of the Arrhenius-like form $k(T) = \alpha (T/300 \text{ K})^\beta \exp(-\gamma/T)$ to the calculated reaction rates.

Reaction	α ($\text{cm}^3 \text{ s}^{-1}$)	β	γ (K)
$SH^+ + H_2 (v=1) \rightarrow H_2S^+ + H$	$4.97\text{e-}11$	0	$1973.4^{(a)}$
$SH^+ + H_2 (v=2) \rightarrow H_2S^+ + H$	$5.31\text{e-}10$	-0.17	$0^{(a)}$
$SH^+ + H_2 (v=3) \rightarrow H_2S^+ + H$	$9.40\text{e-}10$	-0.16	$0^{(a)}$
$SH^+ + H \rightarrow S^+ + H_2$	$1.86\text{e-}10$	-0.41	$27.3^{(b)}$
$SH^+ + e^- \rightarrow S + H$	$2.00\text{e-}07$	-0.50	$^{(c)}$
$H_2S^+ + H \rightarrow SH^+ + H_2$	$6.15\text{e-}10$	-0.34	$0^{(a)}$
$S + H_2 (v=2) \rightarrow SH + H$	$\sim 8.6\text{e-}13$	~ 2.3	$\sim 2500^{(a)}$
$S + H_2 (v=3) \rightarrow SH + H$	$\sim 1.7\text{e-}12$	~ 2.0	$\sim 1500^{(a)}$
$SH + H \rightarrow S + H_2$	$5.7\text{e-}13$	2.48	$1600^{(a, \dagger)}$
	$7.7\text{e-}14$	0.39	$-1.3^{(a, \dagger)}$
$S^+ + H_2 (v=2) \rightarrow SH^+ + H$	$2.88\text{e-}10$	-0.15	$42.9^{(b)}$
$S^+ + H_2 (v=3) \rightarrow SH^+ + H$	$9.03\text{e-}10$	-0.11	$26.2^{(b)}$
$S^+ + H_2 (v=4) \rightarrow SH^+ + H$	$1.30\text{e-}09$	-0.04	$40.8^{(b)}$
$S^+ + H_2 (v=5) \rightarrow SH^+ + H$	$1.21\text{e-}09$	0.09	$34.5^{(b)}$

Notes. ^(a)This work. ^(b)From Zanchet et al. (2019). ^(c)From Prasad & Huntress (1980). ^(†)Total rate is the sum of the two expressions.

detection of bright H_2S emission in the Orion Bar (Figs. 1 and 4) might suggest that subsequent hydrogen abstraction reactions with $H_2 (v \geq 2)$ proceed as well. Motivated by these findings, and before carrying out any PDR model, we studied reaction (2) and the reverse process in detail. This required to build a full dimensional quantum PES of the $H_3S^+ (X^1A_1)$ system (see Appendix A).

In addition, we studied reaction (4) (and its reverse) through quantum calculations. Details of these ab initio calculations and of the resulting reactive cross sections are given in Appendix B. Table 1 summarizes the updated reaction rate coefficients that we will include later in our PDR models.

The H_2S^+ formation rate through reaction (2) with $H_2 (v=0)$ is very slow. For $H_2 (v=1)$, the rate constant increases at $\sim 500 \text{ K}$, corresponding to the opening of the $H_2S^+ + H$ threshold. For $H_2 (v=2)$ and $H_2 (v=3)$, the reaction rate is much faster, close to the Langevin limit (see Appendix A.2). However, our estimated vibrational-state specific rates for SH formation through reaction (4) ($S + H_2$) are considerably smaller than for reactions (1) and (2), and show an energy barrier even for $H_2 (v=2)$ and $H_2 (v=3)$. We anticipate that this reaction is not a relevant formation route for SH .

In FUV-illuminated environments, collisions with H atoms are very important because they compete with electron recombinations in destroying molecular ions, and also they contribute to their excitation. An important result of our calculations is that the destruction rate of H_2S^+ (SH^+) in reactions with H atoms are a factor of ≥ 3.5 (≥ 1.7) faster (at $T_k \leq 200 \text{ K}$) than those previously used in astrochemical models (Millar et al. 1986). Conversely, we find that destruction of SH in reactions with H atoms (Appendix B) is slower than previously assumed.

6. PDR models of S-bearing hydrides

We now investigate the chemistry of S-bearing hydrides and the effect of the new reaction rates in PDR models adapted to the

⁶ If one considers H_2 rovibrational levels, reaction (1) becomes exoergic for $v=0, J \geq 11$ and for $v=1, J \geq 7$ (Zanchet et al. 2019).

The diagram illustrates the reaction network for the formation of molecular hydrogen (H₂) and its subsequent reactions on a grain surface. It is divided into two main regions: Gas-phase (top) and Grain surface (bottom).

Gas-phase reactions:

- S⁺ to SH⁺:** H₂ (9860 K) addition; H-atom abstraction.
- SH⁺ to H₂S⁺:** H₂ (6380 K) addition; H-atom abstraction.
- H₂S⁺ to H₃S⁺:** H₂ (2900 K) addition; H-atom abstraction.
- S⁺ to S:** γ (photoionization).
- S to SH:** H₂ (10500 K) addition; H (700 K) addition; γ (photoionization).
- SH to H₂S:** H₂ (6860 K) addition; H (455 K) addition; γ (photoionization).
- S to SH⁺:** H₃⁺ addition; e⁻ addition.
- SH to S:** e⁻ addition.
- H₂S to H₂S⁺:** S addition; e⁻ addition.
- H₃S⁺ to H₂S:** S addition; e⁻ addition.

Grain surface reactions:

- Adsorption:** S (gas) → s-S.
- Photodesorption:** s-S → S (gas) (γ); s-SH → SH (gas) (γ); s-H₂S → H₂S (gas) (γ).
- Chemical Desorption:** s-SH → SH (gas) (S-H); s-H₂S → H₂S (gas) (S-H).
- Surface Reactions:** s-S → s-SH → s-H₂S.

state-dependent quantum rates for reaction (1) enhances the formation of SH^+ in a narrow layer at the edge of the PDR ($A_V \simeq 0$ to 2 mag). This agrees with the morphology of the SH^+ emission revealed by ALMA images (Fig. 3). For H_2 ($v = 2$), the reaction rate enhancement with respect to the thermal rate $\Delta k = k_2(T)/k_0(T)$ (see discussion by Agúndez et al. 2010) is about 4×10^8 at $T_k = 500$ K (Millar et al. 1986). Indeed, when the fractional abundance of H_2 ($v = 2$) with respect to H_2 ($v = 0$), defined as $f_2 = n(\text{H}_2 v = 2)/n(\text{H}_2 v = 0)$, exceeds a few times 10^{-9} , meaning $\Delta k \cdot f_2 > 1$, reaction (1) with H_2 ($v \geq 2$) dominates SH^+ formation. This reaction enhancement takes place only at the edge of the PDR, where FUV-pumped H_2 ($v \geq 2$) molecules are abundant enough (gray dashed curves in Fig. 12) and drive the formation of SH^+ . The resulting SH^+ column density increases by an order of magnitude compared to models that use the thermal rate.

In this isobaric model, the SH^+ abundance peak occurs at $A_V \approx 0.7$ mag, where the gas density has increased from $n_H \approx 6 \times 10^4 \text{ cm}^{-3}$ at the PDR edge (the IF) to $\sim 5 \times 10^5 \text{ cm}^{-3}$ (at the DF). At this point, SH^+ destruction is dominated by recombination with electrons and by reactive collisions with H atoms. This implies $D(\text{SH}^+) [\text{s}^{-1}] \sim n_e k_e \approx n_H k_H \gg n(\text{H}_2 v \geq 2) k_2$, as we assumed in the single-slab SH^+ excitation models (Sect. 4.1). Therefore, only a small fraction

Model parameter	Value	Note
FUV illumination, G_0	2×10^4 Habing	(a)
Total depth A_V	10 mag	
Thermal pressure P_{th}/k	$2 \times 10^8 \text{ cm}^{-3}\text{K}$	
Density $n_{\text{H}} = n(\text{H}) + 2n(\text{H}_2)$	$n_{\text{H}} = P_{\text{th}} / kT_{\text{k}}$	Varying
Cosmic ray ζ_{CR}	$10^{-16} \text{ H}_2 \text{ s}^{-1}$	(b)
$R_V = A_V/E_{B-V}$	5.5	Orion ^(c)
$M_{\text{gas}}/M_{\text{dust}}$	100	Local ISM
Abundance O/H	3.2×10^{-4}	
Abundance C/H	1.4×10^{-4}	Orion ^(d)
Abundance S/H	1.4×10^{-5}	Solar ^(e)

Orion Bar conditions. In this analysis we used version 1.5.4. of the Meudon PDR code (Le Petit et al. 2006; Bron et al. 2014). Following our previous studies, we model the Orion Bar as a stationary PDR at constant thermal-pressure (i.e., with density and temperature gradients). When compared to time-dependent hydrodynamic PDR models (e.g., Hosokawa & Inutsuka 2006; Bron et al. 2018; Kirsanova & Wiebe 2019), stationary isobaric models seem a good description of the most exposed and compressed gas layers of the PDR, from $A_V \approx 0.5$ to ≈ 5 mag (Goicoechea et al. 2016; Joblin et al. 2018).

In our models, the FUV radiation field incident at the PDR edge is $G_0 = 2 \times 10^4$ (e.g., [Marconi et al. 1998](#)). We adopted an extinction to color-index ratio, $R_V = A_V/E_{B-V}$, of 5.5 ([Joblin et al. 2018](#)), consistent with the flatter extinction curve observed in Orion ([Lee 1968](#); [Cardelli et al. 1989](#)). This choice implies slightly more penetration of FUV radiation into the cloud (e.g., [Goicoechea & Le Bourlot 2007](#)). The main input parameters and elemental abundances of these PDR models are summarized in Table 2. Figure 10 shows the resulting H_2 , H, and electron density profiles, as well as the T_k and T_d gradients.

Our chemical network is that of the Meudon code updated with the new reaction rates listed in Table 1. This network includes updated photoreaction rates from Heays et al. (2017). To increase the accuracy of our abundance predictions, we included the explicit integration of wavelength-dependent SH, SH⁺, and H₂S photodissociation cross sections (σ_{diss}), as well as SH and H₂S photoionization cross sections (σ_{ion}). These cross sections are shown in Fig. C.1. The integration is performed over the specific FUV radiation field at each position of the PDR. In particular, we took $\sigma_{\text{ion}}(\text{SH})$ from Hrodmarsson et al. (2019) and $\sigma_{\text{diss}}(\text{H}_2\text{S})$ from Zhou et al. (2020), both determined in laboratory experiments. Figure 11 summarizes the relevant chemical network that leads to the formation of S-bearing hydrides and that we discuss in the following sections.

6.1. Pure gas-phase PDR model results

Figure 12 shows results of the “new gas-phase” model using the reaction rates in Table 1. The continuous curves display the predicted fractional abundance profiles as a function of cloud depth in magnitudes of visual extinction (A_V). The dashed curves are for a model that uses the standard thermal rates previously adopted in the literature (see, e.g., Neufeld et al. 2015). As noted by Zanchet et al. (2013a, 2019), the inclusion of H_2 ($v \geq 2$)

Table 3. Column density predictions from different PDR models (up to $A_V = 10$ mag) and estimated values from observations (single-slab approach).

Type of PDR model ^(a)	$\log N(\text{cm}^{-2})$ SH ⁺	SH	H ₂ S	H ₂ S ⁺	H ₃ S ⁺
Standard gas-phase	11.0 ^(a) –12.2 ^(b)	11.4 ^(a) –12.5 ^(b)	11.3 ^(a) –12.4 ^(b)	9.9 ^(a) –11.1 ^(b)	7.8 ^(a) –9.0 ^(b)
New gas-phase (Table 1)	12.1 ^(a) –13.2 ^(b)	11.4 ^(a) –12.5 ^(b)	10.6 ^(a) –11.7 ^(b)	9.9 ^(a) –11.0 ^(b)	7.7 ^(a) –8.9 ^(b)
Gas-grain (low E_b , $\epsilon = 1\%$)	12.0 ^(a) –13.2 ^(b)	13.2 ^(a) –14.4 ^(b)	12.9 ^(a) –14.1 ^(b)	9.6 ^(a) –10.7 ^(b)	10.1 ^(a) –11.2 ^(b)
Gas-grain (high E_b , $\epsilon = 1\%$)	12.0 ^(a) –13.1 ^(b)	13.6 ^(a) –14.8 ^(b)	13.7 ^(b) –14.8 ^(b)	9.9 ^(b) –11.0 ^(b)	10.8 ^(b) –12.0 ^(b)
Estimated from observations	~ 13.1	< 13.8	~ 14.4	–	< 10.7

Notes. ^(a)Column densities for a face-on PDR. ^(b)Edge-on PDR with a tilt angle $\alpha = 4^\circ$, leading to the maximum expected geometrical enhancement.

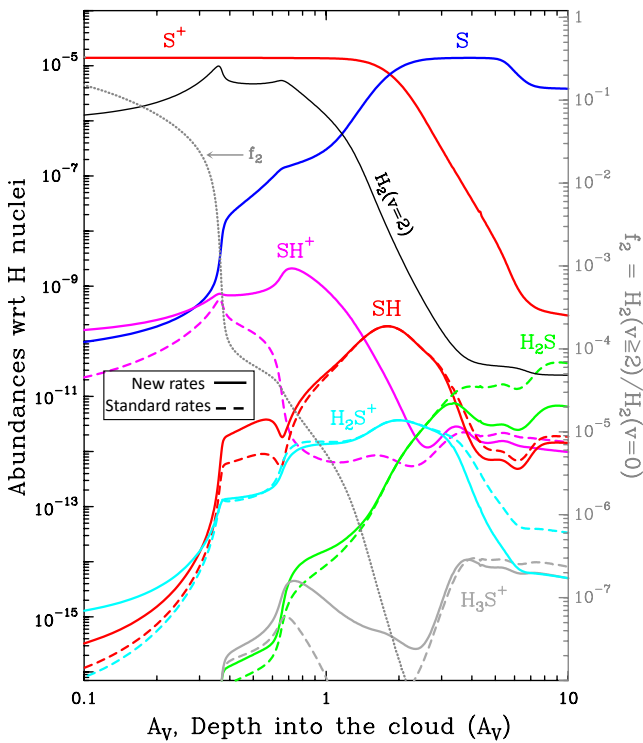


Fig. 12. Pure gas-phase PDR models of the Orion Bar. Continuous curves show fractional abundances as a function of cloud depth, in logarithm scale to better display the irradiated edge of the PDR, using the new reaction rates listed in Table 1. The gray dotted curve shows f_2 , the fraction of H_2 that is in vibrationally excited levels $v \geq 2$ (right axis scale). Dashed curves are for a model using standard reaction rates.

of SH^+ molecules further react with H_2 ($v \geq 2$) to form H_2S^+ . The resulting low H_2S^+ abundances limit the formation of abundant SH from dissociative recombinations of H_2S^+ (recall that we estimated that reaction $\text{S} + \text{H}_2$ ($v \geq 2$) \rightarrow $\text{SH} + \text{H}$ is very slow). The SH abundance peak is shifted deeper inside the cloud, at about $A_V \approx 1.8$ mag, where SH forms by dissociative recombination of H_2S^+ and it is destroyed by FUV photons and reactions with H atoms. In these gas-phase models the H_2S abundance peaks even deeper inside the PDR, at $A_V \approx 5$ mag, where it forms by recombinations of H_2S^+ and H_3S^+ with electrons as well as by charge exchange $\text{S} + \text{H}_2\text{S}^+$. However, the new rate of reaction $\text{H}_2\text{S}^+ + \text{H}$ is higher than assumed in the past, so the new models predict lower H_2S^+ abundances at intermediate PDR depths (thus, less H_3S^+ and H_2S ; see Fig. 12).

The SH column density predicted by the new gas-phase model is below the upper limit determined from SOFIA.

However, the predicted H_2S column density is much lower than the value we derive from observations (Table 3) and the predicted H_2S line intensities are too faint (see Sect. 6.4).

Because the cross sections of the different H_2S photodissociation channels have different wavelength dependences (Zhou et al. 2020), the H_2S and SH abundances between $A_V \approx 2$ and 6 mag are sensitive to the specific shape of the FUV radiation field (determined by line blanketing, dust absorption, and grain scattering; e.g., Goicoechea & Le Boulart 2007). Still, we checked that using steeper extinction curves does not increase H_2S column density any closer to the observed levels. This disagreement between the observationally inferred $N(\text{H}_2\text{S})$ column density and the predictions of gas-phase PDR models is even worse⁷ if one considers the uncertain rates of radiative association reactions $\text{S}^+ + \text{H}_2 \rightarrow \text{H}_2\text{S}^+ + h\nu$ and $\text{SH}^+ + \text{H}_2 \rightarrow \text{H}_3\text{S}^+ + h\nu$ included in the new gas-phase model. For the latter reaction, the main problem is that the electronic states of the reactants do not correlate with the 1A_1 ground electronic state of the activated complex H_3S^{+*} (denoted by *). Instead, H_3S^{+*} forms in an excited triplet state (3A). Herbst et al. (1989) proposed that a spin-flip followed by a radiative association can occur in interstellar conditions and form $\text{H}_3\text{S}^{+*}(X^1A_1)$ (Millar & Herbst 1990). In Appendix A.3, we give arguments against this mechanism. For similar reasons, Prasad & Huntress (1982) avoided to include the $\text{S}^+ + \text{H}_2$ radiative association in their models. Removing these reactions in pure gas-phase models drastically decreases the H_2S^+ and H_3S^+ abundances, and thus those of SH and H_2S (by a factor of ~ 100 in these models). The alternative H_2S^+ formation route through reaction $\text{SH}^+ + \text{H}_2$ ($v = 2$) is only efficient at the PDR surface ($A_V < 1$ mag). This is due to the large H_2 ($v = 2$) fractional abundances, $f_2 > 10^{-6}$ at $T_k > 500$ K, required to enhance the H_2S^+ production. Therefore, and contrary to S^+ destruction, reaction of SH^+ with H_2 is not the dominant destruction pathway for SH^+ . Only deeper inside the PDR, reactions of S with H_3^+ produce small abundances of SH^+ and H_2S^+ , but the hydrogenation of H_nS^+ ions is not efficient and limits the gas-phase production of H_2S .

6.2. Grain surface formation of solid H_2S

Similarly to the formation of water ice (s- H_2O) on grains (e.g., Hollenbach et al. 2009, 2012), the formation of H_2S may be dominated by grain surface reactions followed by desorption back to the gas (e.g., Charnley 1997). Indeed, water vapor is relatively abundant in the Bar ($N(\text{H}_2\text{O}) \approx 10^{15} \text{ cm}^{-2}$; Choi et al. 2014; Putaud et al. 2019) and large-scale maps show that the H_2O abundance peaks close to cloud surfaces (Melnick et al. 2020).

⁷ Older gas-phase PDR models previously predicted low H_2S column densities (Jansen et al. 1995; Sternberg & Dalgarno 1995).

Table 4. Adopted binding energies and photodesorption yields.

Species	E_b/k (K)	Yield (FUV photon) $^{-1}$
S	1100 ^(a) /2600 ^(b)	10^{-4}
SH	1500 ^(a) /2700 ^(b)	10^{-4}
H ₂ S	2700 ^(b,c)	1.2×10^{-3} ^(d) (as H ₂ S)
CO	1300 ^(e)	3×10^{-3} ^(f)
O	1800 ^(g)	10^{-4} ^(f)
O ₂	1200 ^(e)	10^{-3} ^(f)
OH	4600 ^(a)	10^{-3} ^(f)
H ₂ O	4800 ^(h)	10^{-3} ^(f) (as H ₂ O) 2×10^{-3} ^(f) (as OH)

References. ^(a)Hasegawa & Herbst (1993). ^(b)Wakelam et al. (2017). ^(c)Collings et al. (2004). ^(d)Fuente et al. (2017). ^(e)Minissale et al. (2016). ^(f)See, Hollenbach et al. (2009). ^(g)He et al. (2015). ^(h)Sandford & Allamandola (1988).

To investigate the s-H₂S formation on grains, we updated the chemical model by allowing S atoms to deplete onto grains as the gas temperature drops inside the molecular cloud (for the basic grain chemistry formalism, see, Hollenbach et al. 2009). The timescale of this process ($\tau_{gr,S}$) goes as $x(S)^{-1} n_H^{-1} T_k^{-1/2}$, where $x(S)$ is the abundance of neutral sulfur atoms with respect to H nuclei. In a PDR, the abundance of H atoms is typically higher than that of S atoms⁸ and H atoms stick on grains more frequently than S atoms unless $x(H) < x(S) \cdot 0.18$. An adsorbed H atom (s-H) is weakly bound, mobile, and can diffuse throughout the grain surface until it finds an adsorbed S atom (s-S). If the timescale for a grain to be hit by a H atom ($\tau_{gr,H}$) is shorter than the timescale for a s-S atom to photodesorb ($\tau_{photodes,S}$) or sublimate ($\tau_{subl,S}$) then reaction of s-H with s-S will proceed and form a s-SH radical roughly upon “collision” and without energy barriers (e.g., Tielens & Hagen 1982; Tielens 2010). Likewise, if $\tau_{gr,H} < \tau_{photodes,SH}$ and $\tau_{gr,H} < \tau_{subl,SH}$, a newly adsorbed s-H atom can diffuse, find a grain site with an s-SH radical and react without barriers to form s-H₂S. In these surface processes, a significant amount of S is ultimately transferred to s-H₂S (e.g., Vidal et al. 2017), which can subsequently desorb: thermally, by FUV photons, or by cosmic rays. In addition, laboratory experiments show that the excess energy of certain exothermic surface reactions can promote the direct desorption of the product (Minissale et al. 2016). In particular, reaction s-H + s-SH directly desorbs H₂S with a maximum efficiency of ~60% (as observed in experiments, Oba et al. 2018). Due to the high flux of FUV photons in PDRs, chemical desorption may not always compete with photodesorption. However, it can be a dominant process inside molecular clouds (Garrod et al. 2007; Esplugues et al. 2016; Vidal et al. 2017; Navarro-Almaida et al. 2020).

The photodesorption timescale of an ice mantle is proportional to $Y^{-1} G_0^{-1} \exp(+bA_V)$, where Y is the photodesorption yield (the number of desorbed atoms or molecules per incident photon) and b is a dust-related FUV field absorption factor. The timescale for mantle sublimation (thermal desorption) goes as $\nu_{ice}^{-1} \exp(+E_b/kT_d)$, where ν_{ice} is the characteristic vibrational frequency of the solid lattice, T_d is the dust grain temperature, and E_b/k is the adsorption binding energy of the species

⁸ We only consider the depletion of neutral S atoms. S⁺ ions are expected to be more abundant than S atoms at the edge of the Orion Bar ($A_V \lesssim 2$ mag) where T_k and T_d are too high, and the FUV radiation field too strong, to allow the formation of abundant grain mantles.

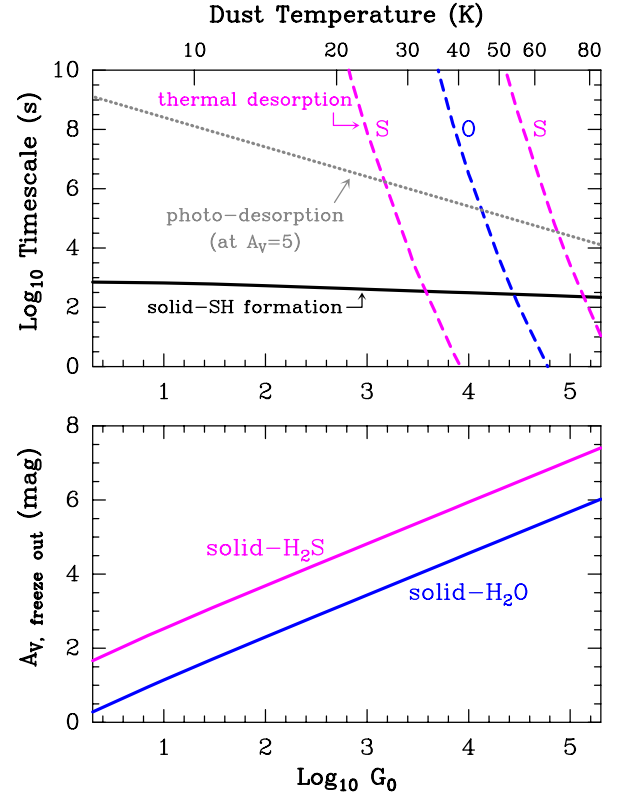


Fig. 13. Representative timescales relevant to the formation of s-H₂S and s-H₂O as well as their freeze-out depths. *Upper panel:* the continuous black curve is the timescale for a grain to be hit by an H atom. Once in the grain surface, the H atom diffuses and can react with an adsorbed S atom to form s-SH. The dashed magenta curves show the timescale for thermal desorption of an s-S atom ($E_b/k(S) = 1100$ K left curve, and 2600 K right curve) and of an s-O atom (blue curve; $E_b/k(O) = 1800$ K). The gray dotted curve is the photodesorption timescale of s-S. At G_0 values where the continuous line is below the dashed and dotted lines, s-O and s-S atoms remain on grain surfaces sufficiently long to combine with an adsorbed H atom and form s-OH and s-SH (and then s-H₂O and s-H₂S). These timescales are for $n_H = 10^5$ cm $^{-3}$ and $n(H) = 100$ cm $^{-3}$. *Bottom panel:* freeze-out depth at which most O and S are incorporated as s-H₂O and s-H₂S (assuming no chemical desorption and $T_k = T_d$).

(in K). Binding energies play a crucial role in model predictions because they determine the freezing temperatures and sublimation timescales. Table 4 lists the E_b/k and Y values considered here.

Representative timescales of the basic grain processes described above are summarized in the upper panel of Fig. 13. In this plot, T_d is a characteristic dust temperature inside the PDR, $T_d = (3 \times 10^4 + 2 \times 10^3 G_0^{1.2})^{0.2}$, taken from Hollenbach et al. (2009). In the upper panel, the continuous black curve is the timescale for a grain to be hit by an H atom ($\tau_{gr,H}$). The dashed magenta curves show the timescale for thermal desorption of an s-S atom ($\tau_{subl,S}$) (left curve for $E_b/k(S) = 1100$ K and right curve for $E_b/k(S) = 2600$ K), and the same for an s-O atom (blue curve). The gray dotted curve is the timescale for s-S atom photodesorption ($\tau_{photodes,S}$) at $A_V = 5$ mag. At G_0 strengths where the continuous line is below the dashed and dotted lines, an adsorbed s-S atom remains on the grain surface sufficiently long to react with a diffusing s-H atom, form s-SH, and ultimately s-H₂S.

Figure 13 shows that, if one takes $E_b/k(S) = 1100$ K (the most common value in the literature; Hasegawa & Herbst 1993), the

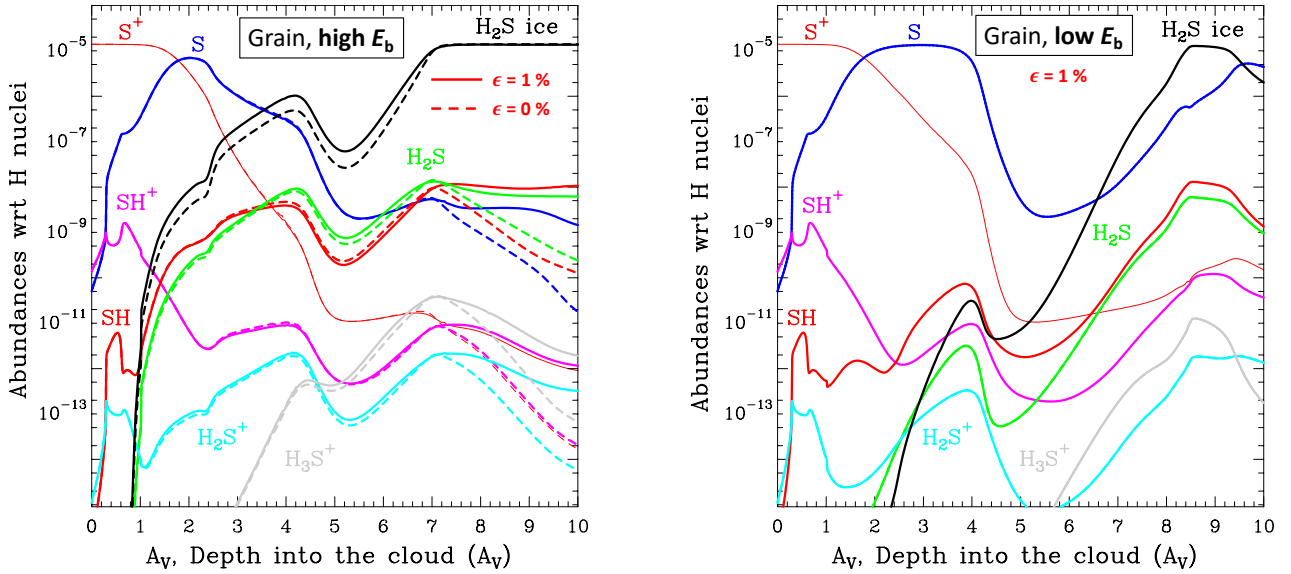


Fig. 14. Gas-grain PDR models leading to the formation of s-H₂S (shown as black curves). Continuous colored curves show gas-phase fractional abundances as a function of depth into the cloud. ϵ refers to the efficiency of the chemical desorption reaction $s\text{-H} + s\text{-H}_2\text{S} \rightarrow \text{SH} + \text{H}_2$ (see text). *Left panel:* gas-grain high E_b model (high adsorption binding energies for S and SH, see Table 4). *Right panel:* low E_b model.

formation of s-H₂S is possible inside clouds illuminated by modest FUV fields, when grains are sufficiently cold ($T_d < 22$ K). However, recent calculations of s-S atoms adsorbed on water ice surfaces suggest higher binding energies (~ 2600 K; Wakelam et al. 2017). This would imply that S atoms freeze at higher T_d ($\lesssim 50$ K) and that s-H₂S mantles form in more strongly illuminated PDRs (the observed T_d at the edge of the Bar is ≈ 50 K and decreases to ≈ 35 K behind the PDR; see, Arab et al. 2012).

The freeze-out depth for sulfur in a PDR, the A_V at which most sulfur is incorporated as S-bearing solids (s-H₂S in our simple model) can be estimated by equating $\tau_{\text{gr}, \text{S}}$ and $\tau_{\text{photdes}, \text{H}_2\text{S}}$. This implicitly assumes the H₂S chemical desorption does not dominate in FUV-irradiated regions, which is in line with the particularly large FUV absorption cross section of s-H₂S measured in laboratory experiments (Cruz-Diaz et al. 2014). With these assumptions, the lower panel of Fig. 13 shows the predicted s-H₂S and s-H₂O freeze-out depths. Owing to the lower abundance and higher atomic mass of sulfur atoms (i.e., grains are hit slower by S atoms than by O atoms), the H₂S freeze-out depth appears slightly deeper than that of water ice. For the FUV-illumination conditions in the Bar, the freeze-out depth of sulfur is expected at $A_V \gtrsim 6$ mag. This implies that photodesorption of s-H₂S can produce enhanced abundances of gaseous H₂S at $A_V < 6$ mag.

FUV-irradiation and thermal desorption of H₂S ice mantles have been studied in the laboratory (e.g., Cruz-Diaz et al. 2014; Jiménez-Escobar & Muñoz Caro 2011). These experiments show that pure s-H₂S ices thermally desorb around 82 K, and at higher temperatures for H₂S–H₂O ice mixtures. These experiments determine a photodesorption yield of $Y_{\text{H}_2\text{S}} \sim 1.2 \times 10^{-3}$ molecules per FUV photon (see also Fuente et al. 2017). Regarding surface grain chemistry, experiments show that reaction $s\text{-H} + s\text{-SH} \rightarrow s\text{-H}_2\text{S}$ is exothermic (Oba et al. 2018), whereas reaction $s\text{-H} + s\text{-H}_2\text{S}$, although it has an activation energy barrier of ~ 1500 K, it may directly desorb gaseous SH. Finally, reaction $s\text{-SH} + s\text{-SH} \rightarrow s\text{-H}_2\text{S}_2$ may trigger the formation of doubly sulfuretted species, but it requires mobile s-SH radicals (e.g., Jiménez-Escobar & Muñoz Caro 2011; Fuente et al. 2017). Here we will only consider surface reactions with mobile s-H.

6.3. Gas-grain PDR model results

Here we show PDR model results in which we add a simple network of gas-grain reactions for a small number of S-bearing (S, SH, and H₂S) and O-bearing (O, OH, H₂O, O₂, and CO) species. These species can adsorb on grains as temperatures drop, photodesorb by FUV photons (stellar and secondary), desorb by direct impact of cosmic-rays, or sublimate at a given PDR depth (depending on T_d and on their E_b). Grain size distributions ($n_{\text{gr}} \propto a^{-3.5}$, where a is the grain radius) and gas-grain reactions are treated within the Meudon code formalism (see, Le Petit et al. 2006; Goicoechea & Le Bourlot 2007; Le Bourlot et al. 2012; Bron et al. 2014). As grain surface chemistry reactions we include $s\text{-H} + s\text{-X} \rightarrow s\text{-XH}$ and $s\text{-H} + s\text{-XH} \rightarrow s\text{-H}_2\text{X}$, where s-X refers to s-S and s-O. In addition, we add the direct chemical desorption reaction $s\text{-H} + s\text{-SH} \rightarrow \text{H}_2\text{S}$ with an efficiency of 50% per reactive event, and also tested different efficiencies (ϵ) for the chemical desorption process $s\text{-H} + s\text{-H}_2\text{S} \rightarrow \text{SH} + \text{H}_2$.

In our models we compute the relevant gas-grain timescales and atomic abundances at every depth A_V of the PDR. If the timescale for a grain to be struck by an H atom ($\tau_{\text{gr}, \text{H}}$) is shorter than the timescales to sublimate or to photodesorb an s-X atom or a s-XH molecule; and if H atoms stick to grains more frequently than X atoms, we simply assume these surface reactions proceed instantaneously. At large A_V , larger than the freeze-out depth, this grain chemistry builds abundant s-H₂O and s-H₂S ice mantles.

Figure 14 shows results of two types of gas-grain models. The only difference between them is the adopted adsorption binding energies for s-S and s-SH. Left panel is for a “high E_b ” model and right panel is for a “low E_b ” model (see Table 4). We note that these models do not include the gas-phase radiative association reactions $\text{S}^+ + \text{H}_2 \rightarrow \text{H}_2\text{S}^+ + h\nu$ and $\text{SH}^+ + \text{H}_2 \rightarrow \text{H}_3\text{S}^+ + h\nu$; although their effect is smaller than in pure gas-phase models.

The chemistry of the most exposed PDR surface layers ($A_V \lesssim 2$ mag) is the same to that of the gas-phase models discussed in Sect. 6.1. Photodesorption keeps dust grains free of ice mantles, and fast gas-phase ion-neutral reactions,

photoreactions, and reactions with FUV-pumped H_2 drive the chemistry. The resulting SH^+ abundance profile is nearly identical and there is no need to invoke depletion of elemental sulfur from the gas-phase to explain the observed SH^+ emission (see Fig. 15). Beyond these first PDR irradiated layers, the chemistry does change because the formation of s- H_2S on grains and subsequent desorption alters the chemistry of the other S-bearing hydrides.

In model high E_b , S atoms start to freeze out closer to the PDR edge ($T_d < 50$ K). Because of the increasing densities and decreasing temperatures, the s- H_2S abundance with respect to H nuclei reaches $\sim 10^{-6}$ at $A_V \simeq 4$ mag. In model low E_b , this level of s- H_2S abundance is only reached beyond an A_V of 7 mag. At lower A_V , the formation of s- H_2S on bare grains and subsequent photodesorption produces more H_2S than pure-gas phase models independently of whether H_2S chemical desorption is included or not. In these intermediate PDR layers, at $A_V \simeq 2\text{--}7$ mag for the strong irradiation conditions in the Bar, the flux of FUV photons drives much of the chemistry, desorbing grain mantles, preventing complete freeze out, and dissociating the gas-phase products.

There are two H_2S abundance peaks at $A_V \simeq 4$ and 7 mag. The H_2S abundance in these “photodesorption peaks” depends on the amount of s- H_2S mantles formed on grains and on the balance between s- H_2S photodesorption and H_2S photodissociation (which now becomes the major source of SH). The enhanced H_2S abundance modifies the chemistry of H_2S^+ and H_3S^+ as well: H_2S photoionization (with a threshold at ~ 10.4 eV) becomes the dominant source of H_2S^+ at $A_V \simeq 4$ mag because the H_2 ($v \geq 2$) abundance is too low to make reaction (2) competitive. Besides, reactions of H_2S with abundant molecular ions such as HCO^+ , H_3^+ , and H_3O^+ dominate the H_3S^+ production.

Our gas-grain models predict that other S-bearing molecules, such as SO_2 and SO , can be the major sulfur reservoirs at these intermediate PDR depths. However, their abundances strongly depend on those of O_2 and OH through reactions $\text{S} + \text{O}_2 \rightarrow \text{SO} + \text{O}$ and $\text{SO} + \text{OH} \rightarrow \text{SO}_2 + \text{H}$ (see e.g., Sternberg & Dalgarno 1995; Fuente et al. 2016, 2019). These reactions link the chemistry of S- and O-bearing neutral molecules (Prasad & Huntress 1982) and are an important sink of S atoms at $A_V \gtrsim 5$ mag. However, while large column densities of OH have been detected in the Orion Bar ($\gtrsim 10^{15} \text{ cm}^{-2}$; Goicoechea et al. 2011), O_2 remains undetected despite deep searches (Melnick et al. 2012). Furthermore, the inferred upper limit $N(\text{O}_2)$ columns are below the expectations of PDR models (Hollenbach et al. 2009). This discrepancy likely implies that these gas-grain models miss details of the grain surface chemistry leading to O_2 (for other environments and modeling approaches see, e.g., Ioppolo et al. 2008; Taquet et al. 2016). Here we will not discuss SO_2 , SO , or O_2 further.

At large cloud depths, $A_V \gtrsim 8$ mag, the FUV flux is largely attenuated, temperatures drop, the chemistry becomes slower, and other chemical processes dominate. The H_2S abundance is controlled by the chemical desorption reaction $\text{s-H} + \text{s-SH} \rightarrow \text{H}_2\text{S}$. This process keeps a floor of detectable H_2S abundances ($> 10^{-9}$) in regions shielded from stellar FUV radiation. In addition, and although not energetically favorable, the chemical desorption $\text{s-H} + \text{s-H}_2\text{S} \rightarrow \text{SH} + \text{H}_2$ enhances the SH production at large A_V (the enhancement depends on the desorption efficiency ϵ), which in turn boosts the abundances of other S-bearing species, including that of neutral S atoms.

The H_2S abundances predicted by the high E_b model reproduce the H_2S line intensities observed in the Bar (Sect. 6.4). In

this model s- H_2S becomes the main sulfur reservoir. However, we stress that here we do not consider the formation of more complex S-bearing ices such as s- OCS , s- H_2S_2 , s- S_n , s- SO_2 or s- HSO (Jiménez-Escobar & Muñoz Caro 2011; Vidal et al. 2017; Laas & Caselli 2019). Together with our steady-state solution of the chemistry, this implies that our predictions are not precise deep inside the PDR. However, we recall that our observations refer to the edge of the Bar, so it is not plausible that the model conditions at $A_V \gtrsim 8$ mag represent the line of sight we observe.

Model low E_b produces less H_2S in the PDR layers below $A_V \lesssim 8$ mag because S atoms do not freeze until the dust temperature drops deep inside the PDR. Even beyond these layers, thermal desorption of s-S maintains higher abundances of S atoms at large depths. Indeed, model low E_b predicts that the major sulfur reservoir deep inside the cloud are gas-phase S atoms. This agrees with recent chemical models of cold dark clouds (Vidal et al. 2017; Navarro-Almida et al. 2020).

6.4. Line intensity comparison and H_2S ortho-to-para ratio

We now specifically compare the SH^+ , SH , and H_2S line intensities implied by the different PDR models with the intensities observed toward the DF position of the Bar. We used the output of the PDR models – T_k , T_d , $n(\text{H}_2)$, $n(\text{H})$, n_e , $n(\text{SH}^+)$, $n(\text{SH})$, and $n(\text{H}_2\text{S})$ profiles from $A_V = 0$ to 10 mag – as input for a multi-slab Monte Carlo model of their line excitation, including formation pumping (formalism presented in Sect. 4) and radiative transfer. As the Orion Bar is not a perfectly edge-on, this comparison requires a knowledge of the tilt angle (α) with respect to a pure edge-on PDR. Different studies suggest α of $\sim 5^\circ$ (e.g., Jansen et al. 1995; Melnick et al. 2012; Andree-Labsch et al. 2017). This inclination implies an increase in line-of-sight column density, compared to a face-on PDR, by a geometrical factor $(\sin \alpha)^{-1}$. It also means that optically thin lines are limb-brightened.

The left panel of Fig. 15 shows SH^+ line intensity predictions for isobaric PDR models of different P_{th} values (leading to different T_k and n_{H} profiles). Since the bulk of the SH^+ emission arises from the PDR edge ($A_V \simeq 0$ to 2 mag) all models (gas-phase or gas-grain) give similar results. The best fit is for $P_{\text{th}} \simeq (1\text{--}2) \times 10^8 \text{ cm}^{-3} \text{ K}$ and $\alpha \simeq 5^\circ$. These high pressures, at least close to the DF, agree with those inferred from ALMA images of HCO^+ ($J=4\text{--}3$) emission (Goicoechea et al. 2016), *Herschel* observations of high- J CO lines (Joblin et al. 2018), and IRAM 30 m detections of carbon recombination lines (Cuadrado et al. 2019).

Right panel of Fig. 15 shows SH and H_2S line emission predictions for the high E_b gas-grain model (magenta squares), low E_b gas-grain model (gray triangles), and a pure gas-phase model (cyan circles). For each model, the upper limit intensities refer to radiative transfer calculations with an inclination angle $\alpha = 5^\circ$. The lower intensity limits refer to a face-on PDR. Gas-phase models largely underestimate the observed H_2S intensities. Model low E_b produces higher H_2S columns and brighter H_2S lines, but still below the observed levels (by up to a factor of ten). Model high E_b provides a good agreement with observations; the two possible inclinations bracket the observed intensities, and it should be considered as the reference model of the Bar. It is also consistent with the observational SH upper limits.

Our observations and models provide a (line-of-sight) $N(o\text{-H}_2\text{S})/N(p\text{-H}_2\text{S})$ OTP ratio of 2.9 ± 0.3 , consistent with the (gas-phase) high-temperature statistical equilibrium value. However, the cold “nuclear-spin-temperatures” ($T_{\text{spin}} \ll T_k$; see definition in Eq. (D.1)) implied by the low water vapor OTP

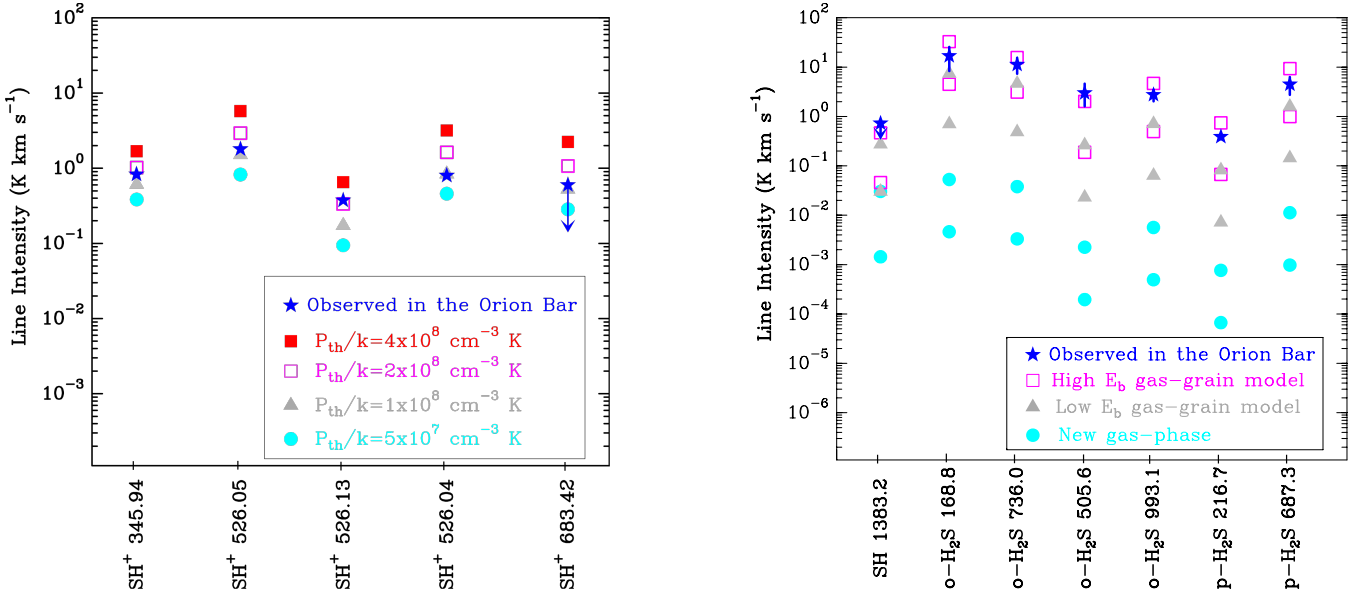


Fig. 15. Line intensity predictions for different isobaric PDR models. Calculations were carried out in a multi-slab Monte Carlo code (Sect. 4) that uses the output of the PDR model. Blue stars show the line intensities observed toward the Bar (corrected by beam dilution). *Left panel:* SH⁺ emission models for PDRs of different P_{th} values and $\alpha = 5^\circ$. *Right panel:* SH and H₂S (adopting an OTP ratio of 3) emission from: high E_b (magenta squares), low E_b (gray triangles), and gas-phase (cyan circles) PDR models, all with $P_{\text{th}}/k = 2 \times 10^8 \text{ K cm}^{-3}$. Upper limit intensity predictions are for a PDR with an inclination angle of $\alpha = 5^\circ$ with respect to a edge-on geometry. Lower limit intensities refer to a face-on PDR model.

ratios observed in some sources (< 2.5) have been associated with the temperature of the ice mantles where H₂O molecules might have formed (i.e., $T_{\text{spin}} \approx T_d$; Mumma et al. 1987; Lis et al. 2013). In the case of H₂S, our derived OTP ratio toward the DF position implies any T_{spin} above $30 \pm 10 \text{ K}$ (see Fig. D.1). Hence, this temperature might be also compatible with s-H₂S formation⁹ in warm grains if $T_{\text{spin}} \approx T_d$ upon formation is preserved in the gas-phase after photodesorption (e.g., Guzmán et al. 2013). Interestingly, the H₂O OTP ratio derived from observations of the Orion Bar is 2.8 ± 0.1 (Putaud et al. 2019) and implies $T_{\text{spin}}(\text{H}_2\text{O}) = 35 \pm 2 \text{ K}$. This value is compatible with $T_{\text{spin}}(\text{H}_2\text{S})$ and might reflect the similar T_d of the PDR layers where most s-H₂O and s-H₂S form and photodesorb. Nevertheless, laboratory experiments have challenged this $T_{\text{spin}} \approx T_d$ association, at least for s-H₂O: cold water ice surfaces, at 10 K, photodesorb H₂O molecules with an OTP ratio of ~ 3 (Hama et al. 2016). Follow up observations of *p*-H₂S lines across the Bar will allow us to study possible variations of the OTP ratio as G_0 diminishes and grains get colder.

6.5. Generalization to different G_0 and n_H conditions

In this section we generalize our results to a broader range of gas densities and FUV illumination conditions (i.e., to clouds with different G_0/n_H ratios). We run several PDR models using the high E_b gas-grain chemistry. The main difference

compared to the Orion Bar models is that here we model constant density clouds with standard interstellar grain properties ($R_V = 3.1$). Figure 16 (left panel) shows models of clouds with constant $n_H = 10^4 \text{ cm}^{-3}$ and varying FUV radiation fields, while Fig. 16 (right panel) show models of constant FUV illumination ($G_0 = 100$) and varying gas densities¹⁰. The main result of this study is the similar gas-phase H₂S column density (a few 10^{14} cm^{-2} up to $A_V = 10$) and H₂S abundance peak (a few 10^{-8} close to the FUV-irradiated cloud edge) predicted by these models nearly irrespective of G_0 and n_H . A similar conclusion was reached previously for water vapor in FUV-illuminated clouds (Hollenbach et al. 2009, 2012). Increasing G_0 shifts the position of the H₂S abundance peak to larger A_V until the rate of S atoms sticking on grains balances the H₂S photodissociation rate (the dominant H₂S destruction mechanism except in shielded gas; see also Fig. 13). Since s-H₂S photodesorption and H₂S photodissociation rates depend on G_0 , the peak H₂S abundance in the PDR is roughly the same independently of G_0 . On the other hand, the formation rate of s-H₂S mantles depends on the product $n(\text{S}) n_{\text{gr}} \propto n_{\text{H}}^2$, whereas the H₂S photodesorption rate depends on $n_{\text{gr}} \propto n_H$. Hence, the H₂S abundance peak moves toward the cloud surface for denser PDRs (like the Orion Bar). The exact abundance value depends on the adopted grain-size distribution and on the H₂S photodesorption yield (which is well constrained by experiments; see, Cruz-Díaz et al. 2014; Fuente et al. 2017).

The role of chemical desorption increases and can dominate beyond the photodesorption peak as the flux of stellar FUV photons is attenuated. Here we do not carry out an exhaustive study of this mechanism, which is hard to model in full detail because its efficiency decreases considerably with the properties of grain surfaces (bare vs. icy; see e.g., Minissale & Dulieu 2014). In our models, and depending on ζ_{CR} , photodesorption by secondary FUV photons can also be important in cloud interiors. These

⁹ Crockett et al. (2014) inferred $N(o\text{-H}_2\text{S})/N(p\text{-H}_2\text{S}) = 2.5 \pm 0.8$ in the hot core of Orion KL using LTE rotational diagrams. However, they favored an OTP ratio of 1.7 ± 0.8 based on the column density ratio of selected pairs of rotational levels with similar energies. This latter OTP ratio implies $T_{\text{spin}}(\text{H}_2\text{S}) \approx 12 \text{ K}$ (Fig. D.1), perhaps related to much colder dust grains than in PDRs or to colder gas conditions just before the hot core phase; so that reactive collisions did not have time to establish the statistical equilibrium value. The observed OTP ratios of H₂CO, H₂CS, and H₂CCO in the Bar are also ~ 3 (Cuadrado et al. 2017).

¹⁰ In these models we consider undepleted [S/H] abundances and only the chemical desorption $s\text{-H} + s\text{-SH} \rightarrow \text{H}_2\text{S}$ (with a 50% efficiency).

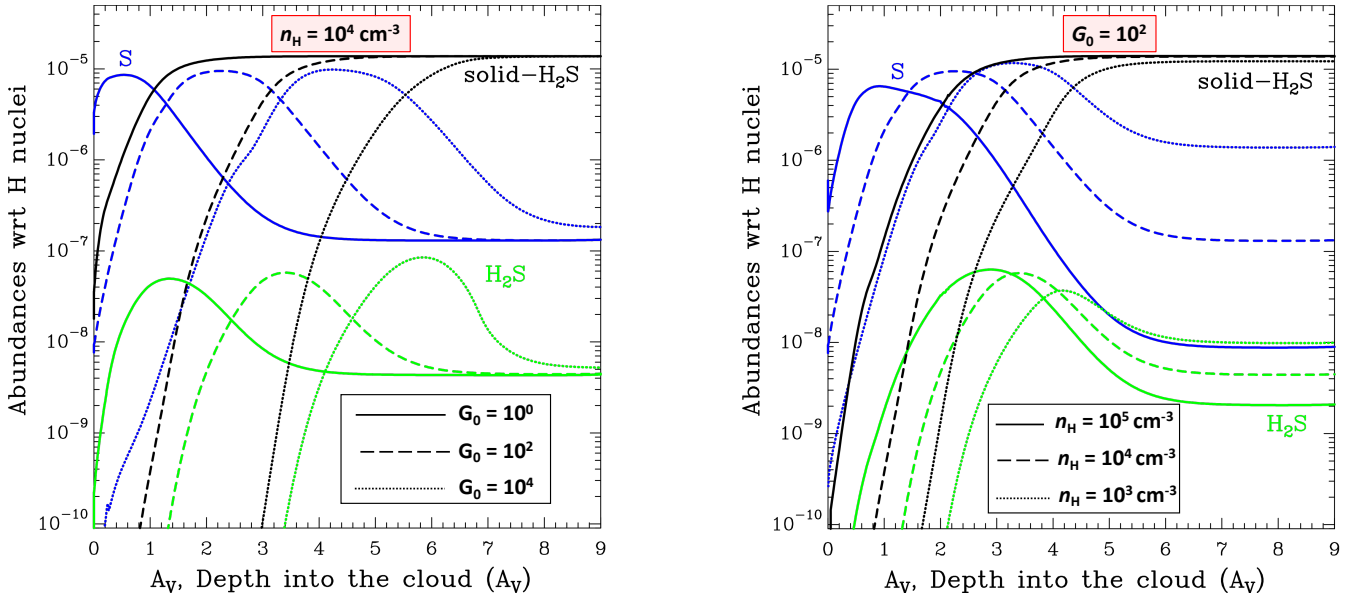


Fig. 16. Constant density gas-grain PDR models using the high E_b chemical network and undepleted sulfur elemental abundances. *Left panel:* effects of changing the FUV radiation field. *Right panel:* effects of varying the gas density.

processes limit the conversion of most of the sulfur reservoir into S-bearing ices and increase the abundance of other gas-phase species deep inside clouds, notably S atoms and H_2S molecules.

The H_2S abundance in shielded gas depends on the destruction rate by gas-phase reactions different than photodissociation, in particular H_2S reactions with H_3^+ . The H_3^+ abundance increases with ζ_{CR} and decreases with the electron density. Figure 16 (right) shows models of constant G_0 and constant ζ_{CR} in which the H_2S abundance at large depths increases with decreasing density (more penetration of FUV photons, more ionization, more electrons, less H_3^+). The lowest gas density model, $n_{\text{H}} = 10^3 \text{ cm}^{-3}$, shows the highest H_2S abundance at large A_V . Because S freeze-out is less efficient at low densities, the low-density model shows higher gas-phase S abundances at large depths, making atomic S a dominant gas-phase sulfur reservoir. Unfortunately, direct observation of atomic S in cold gas is complicated, which makes it difficult to benchmark this prediction.

In warm PDRs, in addition to S radio recombination lines (e.g., Smirnov et al. 1995), the 3P fine-structure lines of atomic sulfur, the [S I] 25, 56 μm lines, can be interesting diagnostics of gas physical conditions and of [S/H] abundances. Unfortunately, the low sensitivity of previous infrared telescopes was not sufficient to detect the [S I] 25 μm line ($\Delta E_{12} = 570 \text{ K}$) in the Orion Bar (Rosenthal et al. 2000); although it is detected in protostellar outflows (e.g., Neufeld et al. 2009; Goicoechea et al. 2012). Moreover, the $^3P_{2-1}D_2$ forbidden line of atomic sulfur at 1.082 μm can be an interesting tracer of the ionization and dissociation fronts in PDRs. Some of these lines will be accessible to high-angular-resolution and high sensitivity observations with JWST.

6.6. The origin of H_2S emission in other environments

Irrespective of n_{H} and G_0 , grain surface formation of s- H_2S and photodesorption back to the gas-phase lead to H_2S column densities of a few 10^{14} cm^{-2} in PDRs. This is in agreement with the observed column in the Bar ($G_0 \approx 10^4$) as well as at the mildly illuminated rims of TMC-1 and Barnard 1b clouds

($G_0 \approx 10$; Navarro-Almaida et al. 2020). The inferred H_2S abundance in the interior of these dark clouds ($A_V > 10 \text{ mag}$) drops to a few 10^{-9} , but the species clearly does not disappear from the gas ($N(\text{H}_2\text{S})$ of a few 10^{13} cm^{-2} ; Navarro-Almaida et al. 2020). Interestingly, neither in the Bar the H_2S line emission at $\sim 168 \text{ GHz}$ decreases much behind the PDR (Fig. 1) even if the flux of FUV photons is largely attenuated compared to the irradiated PDR edge.

Despite oxygen is ~ 25 times more abundant than sulfur, the H_2O to H_2S column density ratio in the Orion Bar PDR is only about ~ 5 . This similarity must also reflect the higher abundances of CO compared to CS. Furthermore, the H_2S column density in cold cores is strikingly similar to that of water vapor (Caselli et al. 2010, 2012). This coincidence points to a more efficient desorption mechanism of s- H_2S compared to s- H_2O in gas shielded from stellar FUV photons. Navarro-Almaida et al. (2020) argues that chemical desorption is able to reproduce the observed H_2S abundance floor if the efficiency of this process diminishes as ice grain mantles get thicker inside cold dense cores.

Turning back to warmer star-forming environments, our predicted H_2S abundance in FUV-illuminated gas is comparable to that observed toward many hot cores ($\sim 10^{-9}$ – 10^{-8} ; van der Tak et al. 2003; Herpin et al. 2009). In these massive protostellar environments, thermal desorption of icy mantles, suddenly heated to $T_d \gtrsim 100 \text{ K}$ by the luminosity of the embedded massive protostar, drives the H_2S production. Early in their evolution, young hot cores ($\lesssim 10^4 \text{ yr}$) can show even higher abundances of recently desorbed H_2S (before further chemical processing takes place in the gas-phase; e.g., Charnley 1997; Hatchell et al. 1998; Jiménez-Serra et al. 2012; Esplugues et al. 2014). Indeed, Crockett et al. (2014) reports a gas-phase H_2S abundance of several 10^{-6} toward the hot core in Orion KL. This high value likely reflects the minimum s- H_2S abundance locked as s- H_2S mantles just before thermal desorption. In addition, the H_2S abundance in the Orion Bar is only slightly lower than that inferred in protostellar outflows (several 10^{-8}). In these regions, fast shocks erode and sputter the grain mantles, releasing a large fraction of their molecular content and activating a high-temperature

gas-phase chemistry that quickly reprocesses the gas (e.g., Holdship et al. 2019). All in all, it seems reasonable to conclude that everywhere s-H₂S grain mantles form, or already formed in a previous evolutionary stage, emission lines from gas-phase H₂S will be detectable.

In terms of its detectability with single-dish telescopes, H₂S rotational lines are bright in hot cores ($T_{\text{peak, 168 GHz}} \approx 30$ K in Orion KL but ≈ 1 –3 K toward most hot cores; Tercero et al. 2010; van der Tak et al. 2003; Herpin et al. 2009), in strongly irradiated PDRs (≈ 6 K, this work), and in lower-illumination PDRs such as the Horsehead (≈ 1 K; Rivière-Marichalar et al. 2019). The H₂S emission is fainter toward cold dark clouds (≈ 0.2 K in TMC-1; Navarro-Almaida et al. 2020) and protostellar outflows (≈ 0.6 K in L1157; Holdship et al. 2019). These line intensity differences are mostly produced by different gas physical conditions and not by enormous changes of the H₂S abundance.

Finally, H₂S is also detected outside the Milky Way (firstly by Heikkilä et al. 1999). Lacking enough spatial-resolution it is more difficult to determine the origin of the extragalactic H₂S emission. The derived abundances in starburst galaxies such as NGC 253 ($\sim 10^{-9}$; Martín et al. 2006) might be interpreted as arising from a collection of spatially unresolved hot cores (Martín et al. 2011). However, hot cores have low filling factors at star-forming cloud scales. Our study suggests that much of this emission can arise from (the most common) extended molecular gas illuminated by stellar FUV radiation (e.g., Goicoechea et al. 2019).

7. Summary and conclusions

We carried out a self-consistent observational and modeling study of the chemistry of S-bearing hydrides in FUV-illuminated gas. We obtained the following results:

- ALMA images of the Orion Bar show that SH⁺ is confined to narrow gas layers of the PDR edge, close to the H₂ dissociation front. Pointed observations carried out with the IRAM 30 m telescope show bright H₂³²S, H₂³⁴S, H₂³³S emission toward the PDR (but no H₃S⁺, a key gas precursor of H₂S) as well as behind the Bar, where the flux of FUV photons is largely attenuated. SOFIA observations provide tight limits to the SH emission.

- The SH⁺ line emission arises from a high-pressure gas component, $P_{\text{th}} \approx (1\text{--}2) \times 10^8 \text{ cm}^{-3} \text{ K}$, where SH⁺ ions are destroyed by reactive collisions with H atoms and electrons (as most H₂S⁺ ions do). We derive $N(\text{SH}^+) \approx 10^{13} \text{ cm}^{-2}$ and an abundance peak of several $\sim 10^{-9}$. H₂S shows larger column densities toward the PDR, $N(\text{H}_2\text{S}) = N(o\text{-H}_2\text{S}) + N(p\text{-H}_2\text{S}) \approx 2.5 \times 10^{14} \text{ cm}^{-2}$. Our tentative detection of SH translates into an upper limit column density ratio $N(\text{SH})/N(\text{H}_2\text{S})$ of $< 0.2\text{--}0.6$, already lower than the ratio of 1.1–3.0 observed in low-density diffuse molecular clouds (Neufeld et al. 2015). This implies an enhanced H₂S production mechanism in FUV-illuminated dense gas.

- All gas-phase reactions $X + \text{H}_2(v=0) \rightarrow \text{XH} + \text{H}$ (with $X = \text{S}^+, \text{S}, \text{SH}^+, \text{or } \text{H}_2\text{S}^+$) are highly endoergic. While reaction of FUV-pumped H₂($v \geq 2$) molecules with S⁺ ions becomes exoergic and explains the observed levels of SH⁺, further reactions of H₂($v \geq 2$) with SH⁺ or with neutral S atoms, both reactions studied here through ab initio quantum calculations, do not form enough H₂S⁺ or H₃S⁺ to ultimately produce abundant H₂S. In particular, pure gas-phase models underestimate the H₂S column density observed in the Orion Bar by more than two orders of magnitude. This implies that these models miss the main H₂S formation route. The disagreement is even worse as we favor, after considering the potential energy surfaces

of the H₂S⁺ and H₃S⁺ complexes, that the radiative associations $\text{S}^+ + \text{H}_2 \rightarrow \text{H}_2\text{S}^+ + h\nu$ and $\text{SH}^+ + \text{H}_2 \rightarrow \text{H}_3\text{S}^+ + h\nu$ may actually not occur or possess slower rates than considered in the literature.

- To overcome these bottlenecks, we built PDR models that include a simple network of gas-grain and grain surface reactions. The higher binding energies of S and SH suggested by recent studies imply that bare grains start to grow s-H₂S mantles not far from the illuminated edges of molecular clouds. Indeed, the observed $N(\text{H}_2\text{S})$ in the Orion Bar can only be explained by the freeze-out of S atoms, grain surface formation of s-H₂S mantles, and subsequent photodesorption back to the gas phase. The inferred H₂S OTP ratio of 2.9 ± 0.3 (equivalent to $T_{\text{spin}} \geq 30$ K) is compatible with the high-temperature statistical ratio as well as with warm grain surface formation if $T_{\text{spin}} \approx T_{\text{d}}$ and if T_{spin} is preserved in the gas-phase after desorption.

- Comparing observations with chemical and excitation models, we conclude that the SH⁺-emitting layers at the edge of the Orion Bar ($A_V < 2$ mag) are characterized by no or very little depletion of sulfur from the gas-phase. At intermediate PDR depths ($A_V < 8$ mag) the observed H₂S column densities do not require depletion of elemental (cosmic) sulfur abundances either.

- We conclude that everywhere s-H₂S grain mantles form (or formed) gas-phase H₂S will be present in detectable amounts. Independently of n_{H} and G_0 , FUV-illuminated clouds produce roughly the same H₂S column density (a few 10^{14} cm^{-2}) and H₂S peak abundances (a few 10^{-8}). This agrees with the H₂S column densities derived in the Orion Bar and at the edges of mildly illuminated clouds. Deep inside molecular clouds ($A_V > 8$ mag), H₂S still forms by direct chemical desorption and photodesorption by secondary FUV photons. These processes alter the abundances of other S-bearing species and makes difficult to predict the dominant sulfur reservoir in cloud interiors.

In this study we focused on S-bearing hydrides. Still, many subtle details remain to be fully understood: radiative associations, electron recombinations, and formation of multiply sulfuretted molecules. For example, the low-temperature ($T_{\text{k}} < 1000$ K) rates of the radiative and dielectronic recombination of S⁺ used in PDR models may still be not accurate enough (Badnell 1991). In addition, the main ice-mantle sulfur reservoirs are not fully constrained observationally. Thus, some of the narrative may be subject to speculation. Similarly, reactions of S⁺ with abundant organic molecules desorbed from grains (such as s-H₂CO, not considered in our study) may contribute to enhance the H₂S⁺ abundance through gas-phase reactions (e.g., $\text{S}^+ + \text{H}_2\text{CO} \rightarrow \text{H}_2\text{S}^+ + \text{CO}$; Prasad & Huntress 1982). Future observations of the abundance and freeze out depths of the key ice carriers with JWST will clearly help in these fronts.

Acknowledgements. We warmly thank Prof. György Lendvai for interesting discussions and for sharing the codes related to their $\text{S}(^3P) + \text{H}_2(^1\Sigma_g^+, v)$ PES. We thank Paul Dagdigan, François Lique, and Alexandre Faure for sharing their H₂S–H₂, SH⁺–H, and SH⁺–e[−] inelastic collisional rate coefficients and for interesting discussions in Grenoble and Salamanca. We thank Helgi Hroddmarsson for sending his experimental SH photoionization cross section in tabulated format. We finally thank our referee, John H. Black, for encouraging and insightful suggestions. This paper makes use of the ALMA data ADS/JAO.ALMA#2012.1.00352.S. ALMA is a partnership of ESO (representing its member states), NSF (USA), and NINS (Japan), together with NRC (Canada), and NSC and ASIAA (Taiwan), in cooperation with the Republic of Chile. The Joint ALMA Observatory is operated by ESO, AUI/NRAO, and NAOJ. It also includes IRAM 30 m telescope observations. IRAM is supported by INSU/CNRS (France), MPG (Germany), and IGN (Spain). We thank the staff at the IRAM 30 m telescope and the work of the USRA and NASA staff of the Armstrong Flight Research Center in Palmdale and of the Ames Research Center in Mountain View (California), and the

Deutsches SOFIA Institut. We thank the Spanish MICIU for funding support under grants AYA2016-75066-C2-2-P, AYA2017-85111-P, FIS2017-83473-C2 PID2019-106110GB-I00, and PID2019-106235GB-I00 and the French-Spanish collaborative project PICS (PIC2017FR). We finally acknowledge computing time at Finisstrae (CESGA) under RES grant ACCT-2019-3-0004.

References

- Aguado, A., & Paniagua, M. 1992, *J. Chem. Phys.*, **96**, 1265
- Aguado, A., Tablero, C., & Paniagua, M. 2001, *Comput. Phys. Comm.*, **134**, 97
- Aguado, A., Barragan, P., Prosmitt, R., et al. 2010, *J. Chem. Phys.*, **133**, 024306
- Agúndez, M., & Wakelam, V. 2013, *Chemical Reviews*, **113**, 8710
- Agúndez, M., Goicoechea, J. R., Cernicharo, J., Faure, A., & Roueff, E. 2010, *ApJ*, **713**, 662
- Allers, K. N., Jaffe, D. T., Lacy, J. H., Draine, B. T., & Richter, M. J. 2005, *ApJ*, **630**, 368
- Anders, E., & Grevesse, N. 1989, *Geochim. Cosmochim. Acta*, **53**, 197
- Andree-Labsch, S., Ossenkopf-Okada, V., & Röllig, M. 2017, *A&A*, **598**, A2
- Anicich, V. G. 2003, *An Index Of The Literature For Bimolecular Gas Phase Cation-Molecule Reaction Kinetics* (California: JPL Publication), 1
- Arab, H., Abergel, A., Habart, E., et al. 2012, *A&A*, **541**, A19
- Asplund, M., Grevesse, N., Sauval, A. J., & Scott, P. 2009, *ARA&A*, **47**, 481
- Azzam, A. A. A., Yurchenko, S. N., Tennyson, J., Martin-Drumel, M.-A., & Piralí, O. 2013, *J. Quant. Spectr. Rad. Transf.*, **130**, 341
- Badnell, N. R. 1991, *ApJ*, **379**, 356
- Bally, J. 2008, *Overview of the Orion Complex*, ed. B. Reipurth (USA: Nasa), 459
- Bañares, L., Aoiz, F. J., Honvault, P., Bussery-Honvault, B., & Launay, J.-M. 2003, *J. Chem. Phys.*, **118**, 565
- Bañares, L., Aoiz, F. J., Honvault, P., & Launay, J.-M. 2004, *J. Phys. Chem.*, **108**, 1616
- Black, J. H. 1998, *Faraday Discuss.*, **109**, 257
- Bonnet, L., & Rayez, J.-C. 1997, *Chem. Phys. Lett.*, **277**, 183
- Bonnet, L., & Rayez, J.-C. 2004, *Chem. Phys. Lett.*, **397**, 106
- Brittain, A., Coolbroth, K., & Boogert, A. 2020, *AAS Meeting Abstracts*, **236**, 247.08
- Bron, E., Le Bourlot, J., & Le Petit, F. 2014, *A&A*, **569**, A100
- Bron, E., Agúndez, M., Goicoechea, J. R., & Cernicharo, J. 2018, ArXiv eprints [arXiv:1801.01547]
- Buckingham, A. D. 1967, *Adv. Chem. Phys.*, **12**, 107
- Burton, M. G., Hollenbach, D. J., & Tielens, A. G. G. M. 1990, *ApJ*, **365**, 620
- Calmonte, U., Altwegg, K., Balsiger, H., et al. 2016, *MNRAS*, **462**, S253
- Cardelli, J. A., Clayton, G. C., & Mathis, J. S. 1989, *ApJ*, **345**, 245
- Caselli, P., Keto, E., Pagani, L., et al. 2010, *A&A*, **521**, L29
- Caselli, P., Keto, E., Bergin, E. A., et al. 2012, *ApJ*, **759**, L37
- Charnley, S. B. 1997, *ApJ*, **481**, 396
- Choi, Y., van der Tak, F. F. S., Bergin, E. A., & Plume, R. 2014, *A&A*, **572**, L10
- Collings, M. P., Anderson, M. A., Chen, R., et al. 2004, *MNRAS*, **354**, 1133
- Crockett, N. R., Bergin, E. A., Neill, J. L., et al. 2014, *ApJ*, **781**, 114
- Cruz-Díaz, G. A., Muñoz Caro, G. M., Chen, Y. J., & Yih, T. S. 2014, *A&A*, **562**, A119
- Cuadrado, S., Goicoechea, J. R., Pilleri, P., et al. 2015, *A&A*, **575**, A82
- Cuadrado, S., Goicoechea, J. R., Roncero, O., et al. 2016, *A&A*, **596**, L1
- Cuadrado, S., Goicoechea, J. R., Cernicharo, J., et al. 2017, *A&A*, **603**, A124
- Cuadrado, S., Salas, P., Goicoechea, J. R., et al. 2019, *A&A*, **625**, L3
- Dagdigian, P. J. 2019a, *MNRAS*, **487**, 3427
- Dagdigian, P. J. 2019b, *J. Chem. Phys.*, **150**, 084308
- Dagdigian, P. J. 2020, *MNRAS*, **494**, 5239
- Dartois, E. 2005, *Space Sci. Rev.*, **119**, 293
- Davidson, E. R. 1975, *J. Comp. Phys.*, **17**, 87
- de Graauw, T., Helmich, F. P., Phillips, T. G., et al. 2010, *A&A*, **518**, L6
- Desrousseaux, B., Lique, F., Goicoechea, J. R., Quintas-Sánchez, E., & Dawes, R. 2021, *A&A*, **645**, A8
- Endres, C. P., Schlemmer, S., Schilke, P., Stutzki, J., & Müller, H. S. P. 2016, *J. Mol. Spectr.*, **327**, 95
- Esplugues, G. B., Viti, S., Goicoechea, J. R., & Cernicharo, J. 2014, *A&A*, **567**, A95
- Esplugues, G. B., Cazaux, S., Meijerink, R., Spaans, M., & Caselli, P. 2016, *A&A*, **591**, A52
- Farah, K., Muller-Plathe, F., & Böhm, M. C. 2012, *Chem. Phys. Chem.*, **13**, 1127
- Faure, A., Halvick, P., Stoecklin, T., et al. 2017, *MNRAS*, **469**, 612
- Freeman, A., & Williams, D. A. 1982, *Ap&SS*, **83**, 417
- Fuente, A., Rodríguez-Franco, A., García-Burillo, S., Martín-Pintado, J., & Black, J. H. 2003, *A&A*, **406**, 899
- Fuente, A., Cernicharo, J., Roueff, E., et al. 2016, *A&A*, **593**, A94
- Fuente, A., Goicoechea, J. R., Pety, J., et al. 2017, *ApJ*, **851**, L49
- Fuente, A., Navarro, D. G., Caselli, P., et al. 2019, *A&A*, **624**, A105
- Garrod, R. T., Wakelam, V., & Herbst, E. 2007, *A&A*, **467**, 1103
- Genzel, R., & Stutzki, J. 1989, *ARA&A*, **27**, 41
- Gerin, M., de Luca, M., Black, J., et al. 2010, *A&A*, **518**, L110
- Gerin, M., Neufeld, D. A., & Goicoechea, J. R. 2016, *ARA&A*, **54**, 181
- Gibb, E. L., Whittet, D. C. B., Boogert, A. C. A., & Tielens, A. G. G. M. 2004, *ApJS*, **151**, 35
- Godard, B., & Cernicharo, J. 2013, *A&A*, **550**, A8
- Godard, B., Falgarone, E., Gerin, M., et al. 2012, *A&A*, **540**, A87
- Godard, B., Falgarone, E., & Pineau des Forêts, G. 2014, *A&A*, **570**, A27
- Goicoechea, J. R., & Le Bourlot, J. 2007, *A&A*, **467**, 1
- Goicoechea, J. R., Pety, J., Gerin, M., et al. 2006, *A&A*, **456**, 565
- Goicoechea, J. R., Pety, J., Gerin, M., Hily-Blant, P., & Le Bourlot, J. 2009, *A&A*, **498**, 771
- Goicoechea, J. R., Joblin, C., Contursi, A., et al. 2011, *A&A*, **530**, L16
- Goicoechea, J. R., Cernicharo, J., Karska, A., et al. 2012, *A&A*, **548**, A77
- Goicoechea, J. R., Pety, J., Cuadrado, S., et al. 2016, *Nature*, **537**, 207
- Goicoechea, J. R., Cuadrado, S., Pety, J., et al. 2017, *A&A*, **601**, L9
- Goicoechea, J. R., Santa-Maria, M. G., Bron, E., et al. 2019, *A&A*, **622**, A91
- Goicoechea, J. R., Pabst, C. H. M., Kabanovic, S., et al. 2020, *A&A*, **639**, A1
- Gómez-Carrasco, S., & Roncero, O. 2006, *J. Chem. Phys.*, **125**, 054102
- Graedel, T. E., Langer, W. D., & Frerking, M. A. 1982, *ApJS*, **48**, 321
- Grozdanov, T. P., & Solov'ev, E. A. 1982, *J. Phys. B*, **15**, 1195
- Guzmán, V. V., Goicoechea, J. R., Pety, J., et al. 2013, *A&A*, **560**, A73
- Habart, E., Dartois, E., Abergel, A., et al. 2010, *A&A*, **518**, L116
- Habing, H. J. 1968, *Bull. Astron. Inst. Netherlands*, **19**, 421
- Hama, T., Kouchi, A., & Watanabe, N. 2016, *Science*, **351**, 65
- Hamilton, J. R., Faure, A., & Tennyson, J. 2018, *MNRAS*, **476**, 2931
- Hasegawa, T. I., & Herbst, E. 1993, *MNRAS*, **261**, 83
- Hatchell, J., Thompson, M. A., Millar, T. J., & MacDonald, G. H. 1998, *A&A*, **338**, 713
- He, J., Shi, J., Hopkins, T., Vidalí, G., & Kaufman, M. J. 2015, *ApJ*, **801**, 120
- Heays, A. N., Bosman, A. D., & van Dishoeck, E. F. 2017, *A&A*, **602**, A105
- Heikkilä, A., Johansson, L. E. B., & Olofsson, H. 1999, *A&A*, **344**, 817
- Herbst, E., DeFrees, D. J., & Koch, W. 1989, *MNRAS*, **237**, 1057
- Herpin, F., Marseille, M., Wakelam, V., Bontemps, S., & Lis, D. C. 2009, *A&A*, **504**, 853
- Heyminck, S., Graf, U. U., Güsten, R., et al. 2012, *A&A*, **542**, L1
- Hogerheijde, M. R., Jansen, D. J., & van Dishoeck, E. F. 1995, *A&A*, **294**, 792
- Holdship, J., Jimenez-Serra, I., Viti, S., et al. 2019, *ApJ*, **878**, 64
- Hollenbach, D. J., & Tielens, A. G. G. M. 1997, *ARA&A*, **35**, 179
- Hollenbach, D., Kaufman, M. J., Bergin, E. A., & Melnick, G. J. 2009, *ApJ*, **690**, 1497
- Hollenbach, D., Kaufman, M. J., Neufeld, D., Wolfire, M., & Goicoechea, J. R. 2012, *ApJ*, **754**, 105
- Hosokawa, T., & Inutsuka, S.-i. 2006, *ApJ*, **646**, 240
- Howk, J. C., Sembach, K. R., & Savage, B. D. 2006, *ApJ*, **637**, 333
- Hrodmarsson, H. R., García, G. A., Nahon, L., Loison, J.-C., & Gans, B. 2019, *Phys. Chem. Chem. Phys.*, **21**, 25907
- Indriolo, N., Neufeld, D. A., Gerin, M., et al. 2015, *ApJ*, **800**, 40
- Ioppolo, S., Cuppen, H. M., Romanzin, C., van Dishoeck, E. F., & Linnartz, H. 2008, *ApJ*, **686**, 1474
- Jansen, D. J., Spaans, M., Hogerheijde, M. R., & van Dishoeck, E. F. 1995, *A&A*, **303**, 541
- Jiménez-Escobar, A., & Muñoz Caro, G. M. 2011, *A&A*, **536**, A91
- Jiménez-Serra, I., Zhang, Q., Viti, S., Martín-Pintado, J., & de Wit, W. J. 2012, *ApJ*, **753**, 34
- Joblin, C., Bron, E., Pinto, C., et al. 2018, *A&A*, **615**, A129
- Johnson, B. R. 1987, *J. Chem. Phys.*, **86**, 1445
- Kaplan, K. F., Dinerstein, H. L., Oh, H., et al. 2017, *ApJ*, **838**, 152
- Karplus, M., Porter, R. N., & Sharma, R. D. 1965, *J. Chem. Phys.*, **43**, 3259
- Kirsanova, M. S., & Wiebe, D. S. 2019, *MNRAS*, **486**, 2525
- Klisch, E., Klaus, T., Belov, S. P., et al. 1996, *ApJ*, **473**, 1118
- Klos, J., Lique, F., & Alexander, M. H. 2009, *Chem. Phys. Lett.*, **476**, 135
- Knizia, G., Adler, T. B., & Werner, H. J. 2009, *J. Chem. Phys.*, **130**, 054104
- Laas, J. C., & Caselli, P. 2019, *A&A*, **624**, A108
- Le Bourlot, J., Le Petit, F., Pinto, C., Roueff, E., & Roy, F. 2012, *A&A*, **541**, A76
- Lee, T. A. 1968, *ApJ*, **152**, 913
- Le Petit, F., Nehmé, C., Le Bourlot, J., & Roueff, E. 2006, *ApJS*, **164**, 506
- Laurini, S., Rolfs, R., Thorwirth, S., et al. 2006, *A&A*, **454**, L47
- Levine, R. D., & Bernstein, R. B. 1987, *Mol Reaction Dynamics and Chemical Reactivity* (Oxford: Oxford University Press)
- Lique, F., Zanchet, A., Bulut, N., Goicoechea, J. R., & Roncero, O. 2020, *A&A*, **638**, A72
- Lis, D. C., Bergin, E. A., Schilke, P., & van Dishoeck, E. F. 2013, *J. Phys. Chem. A*, **117**, 9661
- Lucas, R., & Liszt, H. S. 2002, *A&A*, **384**, 1054
- Maiti, B., Schatz, G. C., & Lendvay, G. 2004, *J. Phys. Chem. A*, **108**, 8772
- Marconi, A., Testi, L., Natta, A., & Walmsley, C. M. 1998, *A&A*, **330**, 696

- Martín, S., Mauersberger, R., Martín-Pintado, J., Henkel, C., & García-Burillo, S. 2006, *ApJS*, **164**, 450
- Martín, S., Krips, M., Martín-Pintado, J., et al. 2011, *A&A*, **527**, A36
- Martin-Drumel, M. A., Eliet, S., Pirali, O., et al. 2012, *Chem. Phys. Lett.*, **550**, 8
- Melnick, G. J., Tolls, V., Goldsmith, P. F., et al. 2012, *ApJ*, **752**, 26
- Melnick, G. J., Tolls, V., Snell, R. L., et al. 2020, *ApJ*, **892**, 22
- Menten, K. M., Wyrowski, F., Belloche, A., et al. 2011, *A&A*, **525**, A77
- Millar, T. J., & Herbst, E. 1990, *A&A*, **231**, 466
- Millar, T. J., Adams, N. G., Smith, D., Lindinger, W., & Villinger, H. 1986, *MNRAS*, **221**, 673
- Minissale, M., & Dulieu, F. 2014, *J. Chem. Phys.*, **141**, 014304
- Minissale, M., Dulieu, F., Cazaux, S., & Hocuk, S. 2016, *A&A*, **585**, A24
- Mumma, M. J., Weaver, H. A., & Larson, H. P. 1987, *A&A*, **187**, 419
- Nagy, Z., & Lendvay, G. 2017, *J. Phys. Chem. Lett.*, **8**, 4621
- Nagy, Z., Van der Tak, F. F. S., Ossenkopf, V., et al. 2013, *A&A*, **550**, A96
- Nagy, Z., Choi, Y., Ossenkopf-Okada, V., et al. 2017, *A&A*, **599**, A22
- Navarro-Almaida, D., Le Gal, R., Fuente, A., et al. 2020, *A&A*, **637**, A39
- Neufeld, D. A., Nisini, B., Giannini, T., et al. 2009, *ApJ*, **706**, 170
- Neufeld, D. A., Goicoechea, J. R., Sonnentrucker, P., et al. 2010, *A&A*, **521**, L10
- Neufeld, D. A., Falgarone, E., Gerin, M., et al. 2012, *A&A*, **542**, L6
- Neufeld, D. A., Godard, B., Gerin, M., et al. 2015, *A&A*, **577**, A49
- Oba, Y., Tomaru, T., Lamberts, T., Kouchi, A., & Watanabe, N. 2018, *Nat. Astron.*, **2**, 228
- O'Dell, C. R. 2001, *ARA&A*, **39**, 99
- Pabst, C., Higgins, R., Goicoechea, J. R., et al. 2019, *Nature*, **565**, 618
- Pabst, C. H. M., Goicoechea, J. R., Teyssier, D., et al. 2020, *A&A*, **639**, A2
- Palumbo, M. E., Geballe, T. R., & Tielens, A. G. G. M. 1997, *ApJ*, **479**, 839
- Pankonin, V., & Walmsley, C. M. 1978, *A&A*, **64**, 333
- Parikka, A., Habart, E., Bernard-Salas, J., et al. 2017, *A&A*, **599**, A20
- Pellegrini, E. W., Baldwin, J. A., Ferland, G. J., Shaw, G., & Heathcote, S. 2009, *ApJ*, **693**, 285
- Peterson, K. A., Adler, T. B., & Werner, H. J. 2008, *J. Chem. Phys.*, **128**, 084102
- Pineau des Forets, G., Flower, D. R., Hartquist, T. W., & Dalgarno, A. 1986, *MNRAS*, **220**, 801
- Prasad, S. S., & Huntress, W. T., Jr. 1980, *ApJS*, **43**, 1
- Prasad, S. S., & Huntress, W. T., Jr. 1982, *ApJ*, **260**, 590
- Putaud, T., Michaut, X., Le Petit, F., Roueff, E., & Lis, D. C. 2019, *A&A*, **632**, A8
- Qu, C., & Bowman, J. M. 2016, *J. Phys. Chem. A*, **120**, 4988
- Rivière-Marichalar, P., Fuente, A., Goicoechea, J. R., et al. 2019, *A&A*, **628**, A16
- Roelfsema, P. R., Helmich, F. P., Teyssier, D., et al. 2012, *A&A*, **537**, A17
- Roncero, O., Zanchet, A., & Aguado, A. 2018, *Phys. Chem. Chem. Phys.*, **20**, 25951
- Rosenthal, D., Bertoldi, F., & Drapatz, S. 2000, *A&A*, **356**, 705
- Sandford, S. A., & Allamandola, L. J. 1988, *Icarus*, **76**, 201
- Sanz-Sanz, C., Roncero, O., Paniagua, M., & Aguado, A. 2013, *J. Chem. Phys.*, **139**, 184302
- Shiozaki, T., & Werner, H.-J. 2013, *Mol. Phys.*, **111**, 607
- Smirnov, G. T., Sorooshenko, R. L., & Walmsley, C. M. 1995, *A&A*, **300**, 923
- Smith, R. G. 1991, *MNRAS*, **249**, 172
- Sofia, U. J., Lauroesch, J. T., Meyer, D. M., & Cartledge, S. I. B. 2004, *ApJ*, **605**, 272
- Stecher, T. P., & Williams, D. A. 1972, *ApJ*, **177**, L141
- Sternberg, A., & Dalgarno, A. 1995, *ApJS*, **99**, 565
- Stoerzer, H., Stutzki, J., & Sternberg, A. 1995, *A&A*, **296**, L9
- Stowe, G. F., Schultz, R. H., Wright, C. A., & Armentrout, P. B. 1990, *Int. J. Mass Spectr. Ion Proc.*, **100**, 377
- Tablero, C., Aguado, A., & Paniagua, M. 2001, *Comput. Phys. Comm.*, **140**, 412
- Taquet, V., Furuya, K., Walsh, C., & van Dishoeck, E. F. 2016, *MNRAS*, **462**, S99
- Tercero, B., Cernicharo, J., Pardo, J. R., & Goicoechea, J. R. 2010, *A&A*, **517**, A96
- Tieftrunk, A., Pineau des Forets, G., Schilke, P., & Walmsley, C. M. 1994, *A&A*, **289**, 579
- Tielens, A. G. G. M. 2010, *The Physics and Chemistry of the Interstellar Medium* (Cambridge: Cambridge University Press)
- Tielens, A. G. G. M., & Hagen, W. 1982, *A&A*, **114**, 245
- Tielens, A. G. G. M., & Hollenbach, D. 1985, *ApJ*, **291**, 722
- Tielens, A. G. G. M., Meixner, M. M., van der Werf, P. P., et al. 1993, *Science*, **262**, 86
- Turner, B. E. 1996, *ApJ*, **468**, 694
- van der Tak, F. F. S., Boonman, A. M. S., Braakman, R., & van Dishoeck, E. F. 2003, *A&A*, **412**, 133
- van der Tak, F. F. S., Black, J. H., Schöier, F. L., Jansen, D. J., & van Dishoeck, E. F. 2007, *A&A*, **468**, 627
- van der Tak, F. F. S., Nagy, Z., Ossenkopf, V., et al. 2013, *A&A*, **560**, A95
- van der Werf, P. P., Stutzki, J., Sternberg, A., & Krabbe, A. 1996, *A&A*, **313**, 633
- van der Werf, P. P., Goss, W. M., & O'Dell, C. R. 2013, *ApJ*, **762**, 101
- van der Wiel, M. H. D., van der Tak, F. F. S., Ossenkopf, V., et al. 2009, *A&A*, **498**, 161
- van Dishoeck, E. F. 2004, *ARA&A*, **42**, 119
- Velilla, L., Lepetit, B., Aguado, A., Beswick, J., & Paniagua, M. 2008, *J. Chem. Phys.*, **129**, 084307
- Vidal, T. H. G., Loison, J.-C., Jaziri, A. Y., et al. 2017, *MNRAS*, **469**, 435
- Wakelam, V., Loison, J. C., Mereau, R., & Ruaud, M. 2017, *Mol. Astrophys.*, **6**, 22
- Walmsley, C. M., Natta, A., Oliva, E., & Testi, L. 2000, *A&A*, **364**, 301
- Werner, H. J., & Knowles, P. J. 1988a, *J. Chem. Phys.*, **89**, 5803
- Werner, H. J., & Knowles, P. J. 1988b, *Chem. Phys. Lett.*, **145**, 514
- Werner, H.-J., Knowles, P. J., Knizia, G., Manby, F. R., & Schütz, M. 2012, *WIREs Comput. Mol. Sci.*, **2**, 242
- Wyrowski, F., Schilke, P., Hofner, P., & Walmsley, C. M. 1997, *ApJ*, **487**, L171
- Yamamura, I., Kawaguchi, K., & Ridgway, S. T. 2000, *ApJ*, **528**, L33
- Young, E. T., Becklin, E. E., Marcum, P. M., et al. 2012, *ApJ*, **749**, L17
- Zanchet, A., Roncero, O., González-Lezana, T., et al. 2009, *J. Phys. Chem. A*, **113**, 14488
- Zanchet, A., Agúndez, M., Herrero, V. J., Aguado, A., & Roncero, O. 2013a, *AJ*, **146**, 125
- Zanchet, A., Godard, B., Bulut, N., et al. 2013b, *ApJ*, **766**, 80
- Zanchet, A., del Mazo, P., Aguado, A., et al. 2018, *PCCP*, **20**, 5415
- Zanchet, A., Lique, F., Roncero, O., Goicoechea, J. R., & Bulut, N. 2019, *A&A*, **626**, A103
- Zhou, J., Zhao, Y., Hansen, C. S., et al. 2020, *Nat. Commun.*, **11**, 1547

Appendix A: H_2S^+ formation and destruction

In this appendix we give details about how we calculated the H_2 vibrational-state-dependent rates of reaction (2) and of the reverse reaction, the destruction of H_2S^+ ($^2\text{A}'$) by reactive collisions with H (^2S) atoms (summarized in Fig. A.1).

We first built a full dimensional potential energy surface (PES) of the triplet H_3S^+ (^3A) system by fitting more than 150 000 ab initio points, including the long range interactions in the reactants and products channels. The main topological features of the PES are summarized in the minimum energy path between reactants and products (see middle panel of Fig. 9). These ab initio points were calculated with an explicitly correlated restricted coupled cluster including a single, double, and (perturbatively) triple excitations (RCCSD(T)-F12a) method (Knizia et al. 2009). The analytical fit has a overall rms error of ≈ 0.01 eV (Fig. A.2). Appendix A.1 provides more details.

Reaction (2) is endothermic by 0.672 eV, and the PES of the triplet state shows two shallow wells in the $\text{H}_2 + \text{SH}^+$ entrance channel (named $^3\text{W}_{1a}$ and $^3\text{W}_{1b}$, with a depth of ≈ 0.118 eV) and another one near the $\text{H} + \text{H}_2\text{S}^+$ products (named $^3\text{W}_2$, with a depth of 0.08 eV). Between the reactants and products wells there is a saddle point, with an energy of 0.601 eV. This saddle point, slightly below the products, has a geometry similar to $^3\text{W}_2$ in which the H–H distance is strongly elongated compared to that of H_2 . These features are also present in the maximum multiplicity PES of reactions $\text{H}_2 + \text{S}^+$ (^4S) and $\text{H}_2 + \text{H}_2\text{S}^+$ (^2A) (see Fig. 9). We determine the state-dependent rates of reaction (2) and of the reverse reaction using a quasi-classical trajectory (QCT) method on our ground triplet PES. We provide more details on how the reactive cross sections for fixed collision energies were calculated in Appendix A.2.

The formation rate of H_2S^+ from H_2 ($v=0$) is very slow. For H_2 ($v=1$), the rate constant significantly increases at ≈ 500 K, corresponding with the opening of the $\text{H}_2\text{S}^+ + \text{H}$ threshold. At this point, it is important to consider the zero-point energy (ZPE) of the products (see next section for details). For H_2 ($v=2$) and H_2 ($v=3$), reaction rates are faster, close to the Langevin limit. Finally, the H_2S^+ destruction rate constant is very similar to that of its formation from H_2 ($v=2$). In Appendix A.3 we provide more information about the destruction of H_nS^+ ions through radiative association and spin flip mechanisms.

A.1. Ab initio calculations and PES

Dagdikian (2019b) presented a PES for the $\text{SH}^+ - \text{H}_2$ system that includes 4-dimensions and is based on RCCSD(T)-F12a ab initio calculations. This PES was used to study $\text{SH}^+ - \text{H}_2$ inelastic collisions using a rigid rotor approach in which the two diatomic molecules are kept fixed at their equilibrium distances. However, in order to study the reactivity of the collision, the two diatomic distances have to be included to account for the breaking and formation of new bonds.

Reaction (2) corresponds to a triplet state H_3S^+ (^3A). The H_2S^+ ($^2\text{A}'$) + H (^2S) products can form a triplet and a singlet state. The triplet state can lead to the destruction of H_2S^+ through reaction with H atoms. The singlet state, however, produces very excited states of the reactants. Thus, it only leads to inelastic collisions but not to the destruction of H_2S^+ ($^2\text{A}'$). In consequence, here we only consider the ground triplet electronic state of the system. In addition, the $\text{H}_3^+ + \text{S}$ (^3P) channel is about 2.4 eV above the $\text{H}_2 + \text{SH}^+$ asymptote, and will not be included in the present study.

In order to study the regions where several electronic states intersect, we performed a explicitly correlated internally

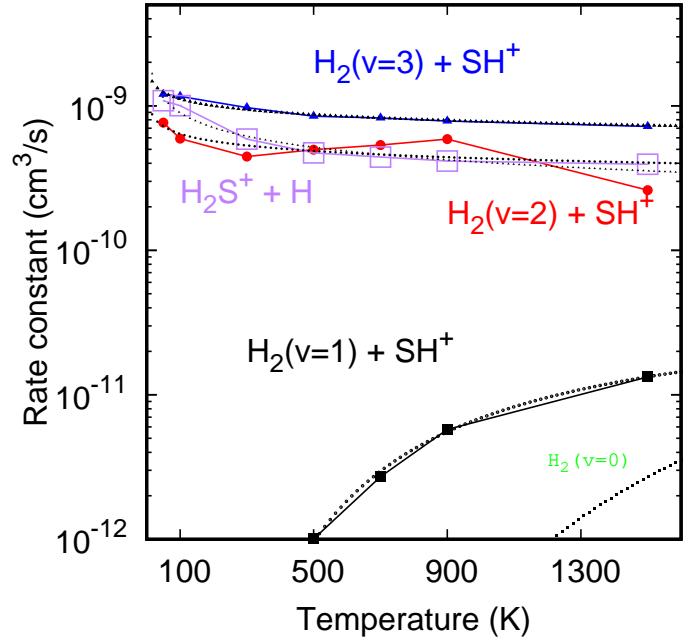


Fig. A.1. Calculated rate constants as a function of temperature (for translation and rotation) for SH^+ ($v=0, j=0$) + H_2 ($v=1, 2, 3, j=0$) and H_2S^+ ($v=0, j=0$) + H reactions (lavender) using ZPE corrected QCT method. Dotted curves are fits of the form $k(T) = \alpha (T/300)^\beta \exp(-\gamma/T)$. Rate coefficients are listed in Table 1.

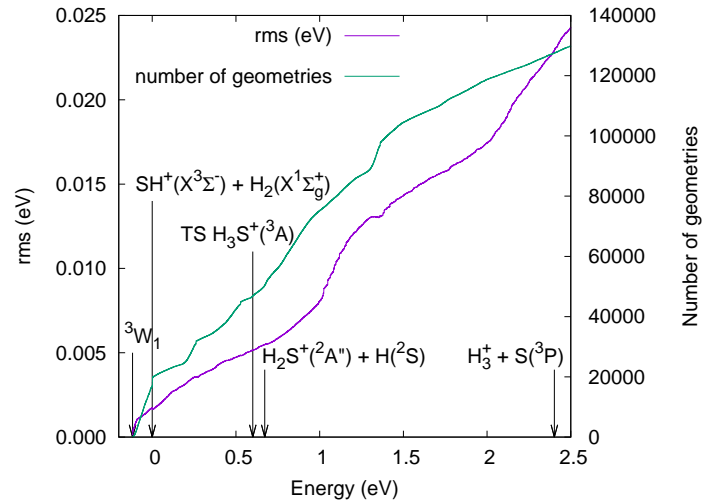


Fig. A.2. Rms error as a function of total energy, showing the number of ab initio points used to evaluate the error in the PES calculation. Arrows indicate selected critical points in the PES and provide an estimate of the error in each region. TS means transition state.

contracted multireference configuration interaction (ic-MRCI-F12) calculation (Shiozaki & Werner 2013; Werner & Knowles 1988a,b) including the Davidson correction (icMRCI-F12+Q; Davidson 1975). The ic-MRCI-F12 calculations were carried out using state-averaged complete active space self-consistent field (SA-CASSCF) orbitals with all the CAS configurations as the reference configuration state functions. We used a triple zeta correlation consistent basis set for explicitly correlated wave functions (cc-pVTZ-F12; Peterson et al. 2008). In order to avoid orbital flipping between core and valence orbitals, SA-CASSCF calculations with three lowest triplet states were carried out

including the core and valence orbitals as active space (18 electrons in 11 orbitals). For the ic-MRCI-F12 calculation, the core orbitals were kept doubly occupied, resulting in about 2.5×10^6 (9×10^7) contracted (uncontracted) configurations. All ab initio calculations were performed with MOLPRO (Werner et al. 2012).

Our ic-MRCI-F12 calculations show that the crossings with electronic excited states are 2 eV above the energy of the reactants. The energy interval below 2 eV is enough to study reaction (2). In these low-energy regions, RCCSD(T)-F12a calculations were also performed. They are in good agreement with the ic-MRCI-F12 results and the t_1 diagnostic is always below 0.03. This allows us to conclude that for energies below 2 eV, the RCCSD(T)-F12a method performs well, presents a simple convergence, and being size consistent, is well adapted to the present case. This method is the same one employed in the inelastic collision calculations by Dagdigian (2019b).

We performed extensive RCCSD(T)-F12a calculations in all accessible regions to properly describe the six-dimensional phase space. 150 000 ab initio points were fitted to a multidimensional analytic function, that generates the six-dimensional PES represented as

$$H = H^{\text{diab}} + H^{\text{MB}} \quad (\text{A.1})$$

(Aguado et al. 2010; Sanz-Sanz et al. 2013; Zanchet et al. 2018; Roncero et al. 2018), where H^{diab} is an electronic diabatic matrix in which each diagonal matrix element describes a rearrangement channel – six in this case, three equivalent for $\text{SH}^+ + \text{H}_2$ channels, and three equivalent for $\text{H}_2\text{S}^+ + \text{H}$ fragments (we omitted the $\text{H}_3^+ + \text{S}$ channel) – as an extension of the reactive force field approach (Farah et al. 2012). In each diagonal term, the molecular fragments (SH^+ , H_2 and H_2S^+) are described by 2 or 3 body fits (Aguado & Paniagua 1992), and the interaction among them is described by a sum of atom-atom terms plus the long range interaction. The non diagonal terms of H^{diab} are described as previously (Zanchet et al. 2018; Roncero et al. 2018) and the parameters are fitted to approximately describe the saddle points along the minimum energy path in the right geometry.

In the reactants channel, the leading long range interaction $\text{SH}^+(X^3\Sigma^-) + \text{H}_2(X^1\Sigma_g^+)$ corresponds to charge-quadrupole and charge-induced dipole interactions (Buckingham 1967):

$$V_{\text{charge}}(\mathbf{r}_{\text{HH}}, \mathbf{R}) = \Theta_2(r_{\text{HH}})P_2(\cos \theta_2)R^{-3} - \left[\frac{1}{2}\alpha_0(r_{\text{HH}}) + \frac{1}{3}(\alpha_{\parallel}(r_{\text{HH}}) - \alpha_{\perp}(r_{\text{HH}}))P_2(\cos \theta_2) \right] R^{-4} \quad (\text{A.2})$$

and the dipole-quadrupole interactions (Buckingham 1967):

$$V_{\text{dipole}}(\mathbf{r}_{\text{SH}}, \mathbf{r}_{\text{HH}}, \mathbf{R}) = 3\mu_1(r_{\text{SH}})\Theta_2(r_{\text{HH}}) \times [\cos \theta_1 P_2(\cos \theta_2) + \sin \theta_1 \sin \theta_2 \cos \theta_2 \cos \phi] R^{-4}, \quad (\text{A.3})$$

where $\Theta_2(r_{\text{HH}})$ is the quadrupole moment of $\text{H}_2(X^1\Sigma_g^+)$, $\alpha_0(r_{\text{HH}})$, $\alpha_{\parallel}(r_{\text{HH}})$, and $\alpha_{\perp}(r_{\text{HH}})$ are the average, parallel, and perpendicular polarizabilities of $\text{H}_2(X^1\Sigma_g^+)$, respectively, and $\mu_1(r_{\text{SH}})$ is the dipole moment of $\text{SH}^+(X^3\Sigma^-)$. $P_2(\cos \theta)$ represents the Legendre polynomial of degree 2. The dependence of the molecular properties of H_2 with the interatomic distance r_{HH} is obtained from Velilla et al. (2008). The dipole moment of SH^+ depends on the origin of coordinates. Since $\text{SH}^+(X^3\Sigma^-)$ dissociates in $\text{S}^+(^4S) + \text{H}(^2S)$, we select the origin of coordinates in the S atom, so that the dipole moment tends to zero when R goes to infinity.

Table A.1. RCCSD(T)-F12a and fit stationary points on the PES.

Stationary point	Geometry	Energy/cm ⁻¹	Energy/eV
Reactants	$\text{SH}^+ + \text{H}_2$	0.0	0.0
Minimum 1	$\text{SH}^+ - \text{H}_2$	-950.2	-0.1178
TS12	$\text{SH}^+ \cdots \text{H}_2$	-579.5	-0.0719
Minimum 2	$\text{SH}^+ - \text{H}_2$	-937.9	-0.1163
TS13	$\text{SH}^+ \cdots \text{H} \cdots \text{H}$	4843.9	0.6006
Minimum 3	$\text{H}_2\text{S}^+ - \text{H}$	4766.5	0.5910
Products	$\text{H}_2\text{S}^+ + \text{H}$	5422.3	0.6723

Table A.2. E_v of reactants and products, and adiabatic switching energies for the QCT initial conditions.

System(vibration)	Exact E_v (eV)	AS energy (eV)
$\text{H}_2(v=0)$	0.270	0.269
$\text{H}_2(v=1)$	0.786	0.785
$\text{H}_2(v=2)$	1.272	1.272
$\text{H}_2(v=3)$	1.735	1.730
$\text{SH}^+(v=0)$	0.157	0.157
$\text{H}_2\text{S}^+(v=0)$	0.389	0.388

In the products channel, the long range interaction $\text{H}_2\text{S}^+(X^2A'') + \text{H}(^2S)$ corresponds to the isotropic charge-induced dipole and charge-induced quadrupole dispersion terms

$$V_{\text{disp}}(R) = -\frac{9}{4}R^{-4} - \frac{15}{4}R^{-6}.$$

These long range terms diverge at $R=0$. To avoid this behavior, we replace R by \mathcal{R} :

$$\mathcal{R} = R + R_0 e^{-(R-R_c)} \quad \text{with} \quad R_0 = 10 \text{ bohr}.$$

In Eq. (A.1), H^{MB} is the many-body term, which is described by permutationally invariant polynomials following the method of Aguado and collaborators (Aguado & Paniagua 1992; Tablero et al. 2001; Aguado et al. 2001). This many-body term improves the accuracy of the PES, especially in the region of the reaction barriers (as shown in Fig. 9). Features of the stationary points are listed in Table A.1.

A.2. Determination of reactive collision rates

We studied the reaction dynamics using a quasi-classical trajectory (QCT) method with the code miQCT (Zanchet et al. 2018; Roncero et al. 2018). In this method, the initial vibrational energy of the reactants is included using the adiabatic switching method (AS) (Grozdanov & Solov'ev 1982; Johnson 1987; Qu & Bowman 2016; Nagy & Lendvay 2017). Energies are listed in Table A.2. The initial distance between the center-of-mass of the reactants ($\text{H}_2 + \text{SH}^+$ or $\text{H}_2\text{S}^+ + \text{H}$) is set to 85 bohr, and the initial impact parameter is set randomly within a disk, the radius of which is set according to a capture model (Levine & Bernstein 1987) using the corresponding long-range interaction. The orientation among the two reactants is set randomly.

A first exploration of the reaction dynamics is done at fixed collision energy, for $\text{H}_2(v=0, 1, 2, 3) + \text{SH}^+(v=0)$ and $\text{H} + \text{H}_2\text{S}^+(v=0)$, and the reactive cross section is calculated as

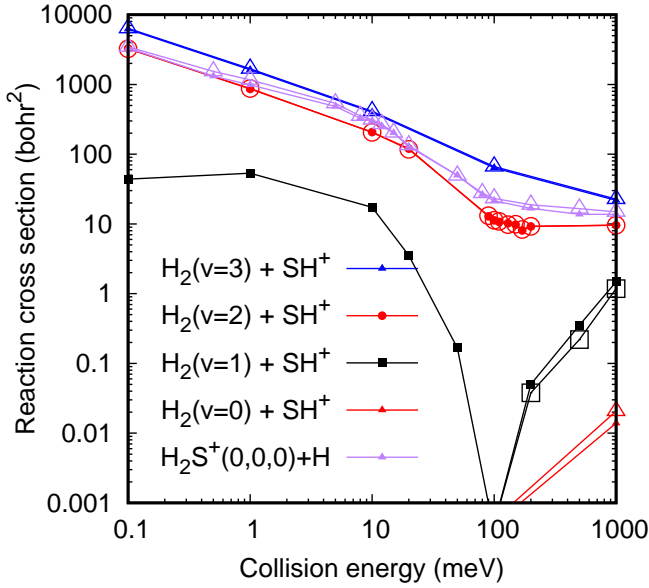


Fig. A.3. Reaction cross section (in bohr²) as a function of collision energy (in meV) for the SH⁺ ($v=0, j=0$) + H₂ ($v=1, 2, 3, j=0$) and H₂S⁺ ($v=0, j=0$) + H collisions. Filled symbols are obtained counting all trajectories leading to products, while open symbols correspond to the ZPE corrected ones.

in Karplus et al. (1965)

$$\sigma_{vj}(E) = \pi b_{\max}^2 P_r(E) \quad \text{with} \quad P_r(E) = \frac{N_r}{N_{\text{tot}}}, \quad (\text{A.4})$$

where N_l is the maximum number of trajectories with initial impact parameter lower than b_{\max} , the maximum impact parameter for which the reaction takes place, and N_r is the number of trajectories leading to products. Figure A.2 shows results for $N_l > 20\,000$ and all energies and initial reactant and vibrational states.

For the SH⁺ ($v=0, j=0$) + H₂ ($v, j=0$) reaction there is a strong dependence on the initial vibrational state. For H₂ ($v=0$), there is nearly no reactive event, and only at 1 eV there are some reactive trajectories. For H₂ ($v=2$ and 3), however, the reaction shows a relatively large cross section, that decreases with increasing collision energy, as expected for exoergic reactions. Energies below 10–100 meV are dominated by long range interactions, leading to an increase in the maximum impact parameter, b_{\max} , consistent with the variation of the cross section.

Reaction SH⁺ ($v=0, j=0$) + H₂ ($v=1, j=0$) shows an unexpected behavior that deserves some discussion. At energies below 40 meV, the cross section is large and decreases with increasing energy. In the 40–200 meV that is consistent with the endothermicity of the reaction.

In order to analyze the reaction mechanism for H₂ ($v=1$) below 40 meV, we carried out an extensive analysis of the trajectories. A typical one is presented in Fig. A.4 for 10 meV. The H₂ and SH⁺ reactants are attracted to each other by long range interactions, until they get trapped in the ³W₁ wells, as it is shown by the evolution of R , the distance between center-of-mass of the two molecules. The trapping lasts for 8 ps, thus allowing several collisions between H₂ and SH⁺ and permitting the energy transfer between them. The H₂ molecule ultimately breaks, and leaves SH⁺ with less vibrational energy. This can be inferred from the decrease in the amplitudes of the SH⁺ distance. The energy of

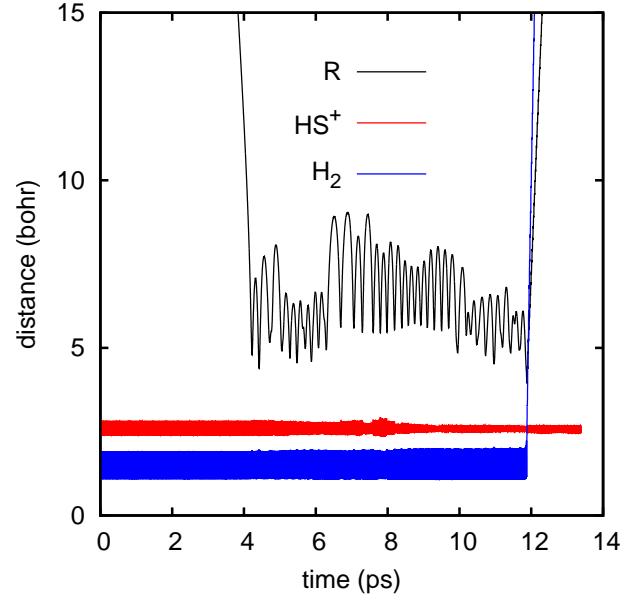


Fig. A.4. H–H, SH⁺ and R distances (in bohr) versus time (in ps), for a typical reactive trajectory for the SH⁺ ($v=0, j=0$) + H₂ ($v=1, j=0$) collision at 10 meV.

the H₂S⁺ product is below the ZPE (see Table A.2). This is a clear indication of ZPE leakage in the QCT method, due to the energy transfer promoted by the long-lived collision complex.

Several methods exist that correct the ZPE leakage. One is the Gaussian binning (Bonnet & Rayez 1997, 2004; Bañares et al. 2003, 2004). Here we have applied a simplification of this method, which assigns a weight (w) for each trajectory as

$$w = \begin{cases} 1 & \text{for } E_{\text{vib}} > \text{ZPE} \\ e^{-\gamma(E_{\text{vib}} - \text{ZPE})^2} & \text{for } E_{\text{vib}} < \text{ZPE} \end{cases}, \quad (\text{A.5})$$

where E_{vib} is the vibrational energy of reactants (adding those of H₂ and SH⁺) or H₂S⁺ products at the end of each trajectory. These new weights are used to calculate N_r and N_{tot} in Eq. (A.4). ZPE-corrected results are shown in Fig. A.3 with open symbols. This plot shows that all values are nearly the same as those calculated simply by counting trajectories as an integer (as done in the normal binning method; see filled symbols in Fig. A.3). The only exception is the case of SH⁺ + H₂ ($v=1$) below 400 meV, which becomes zero when considering the ZPE of fragments at the end of the trajectories.

The reaction thermal rate in specific initial vibrational state of reactants are calculated running a minimum of 10^5 trajectories per temperature, with fixed vibrational states of reactants, assuming a Boltzmann distribution over translational and rotational degrees of freedom, and following the ZPE-corrected method as:

$$k_v(T) = \sqrt{\frac{8k_B T}{\pi \mu}} \pi b_{\max}^2(T) P_r(T). \quad (\text{A.6})$$

The results of these calculations are shown in Fig. A.1.

A.3. On the radiative associations of H_nS⁺

Herbst et al. (1989) and Millar & Herbst (1990) proposed that the radiative association H_nS⁺ + H₂ → H_{n+1}S⁺ + $h\nu$ is viable process at low gas temperatures. Although this chemical route

is widely used in astrochemical models, here we question the viability of this process. The lower multiplicity (L) PESs of H_2S^+ ($^2A''$) and H_3S^+ (1A) are $L = 1/2$ and 0 respectively. These are shown in Fig. 9, together with the minimum multiplicity electronic state of H_4S^+ (bottom panel). This state does not have a deep well or any higher multiplicity state that could connect to higher states of reactants and products.

For of H_3S^+ formation through radiative association, this process assumes that a $\text{H}_3\text{S}^+(^3A)^*$ complex forms in a triplet state, the high spin state H considered here. According to our calculations, such a complex is formed after low-energy $\text{H}_2(v=0, 1) + \text{SH}^+$ reactions (below 40 meV). The complex is formed in the 3W_1 well, corresponding to geometries very far from those of the low spin well, the 1W well. Therefore, a radiative spin flip and decay through phosphorescence is not possible. Herbst et al. (1989) proposed a second step, in which the spin flips from the triplet to the singlet state, followed by a radiative association, finally leading to the $\text{H}_3\text{S}^+(^1A)$ product.

The origin of the spin flip must be the spin-orbit couplings, very relevant for S-bearing species, that favor the spin transition when singlet and triplet states are close in energy. Using the PESs calculated here, the lowest crossing region is at ≈ 0.25 eV, very close to that of $\text{H}_2(v=0)$. At low temperatures, the $\text{H}_3\text{S}^+(^3A)^*$ complex formed by $\text{H}_2(v=0) + \text{SH}^+$ reactions might allow a transition between the two electronic states with different spin. However, the spin flip probability is proportional to the square of the overlap $|\langle \text{H}_3\text{S}^+(^3A)^* | \text{H}_3\text{S}^+(^1A)^* \rangle|^2$. This probability is very small because the two wells, 3W_1 and 1W_1 , correspond to very different geometries. In consequence, we conclude that this radiative association mechanism must be negligible, especially at the high gas temperatures of PDR edges where the $\text{H}_3\text{S}^+(^3A)^*$ complex is not formed.

As an alternative, a spin flip in a direct collision (not forming a $\text{H}_3\text{S}^+(^3A)^*$ complex) may be more efficient and should be further investigated. Indeed, experimental measurements of the $\text{S}^+(^4S) + \text{H}_2(v=0)$ cross section show a maximum at about 1 eV of collisional energy attributed to spin-orbit transitions leading to spin flip (Stowe et al. 1990).

Appendix B: Reaction $\text{S}(^3P) + \text{H}_2(v) \rightleftharpoons \text{SH} + \text{H}$

This reaction involves open shell reactants, $\text{S}(^3P)$, and products, $\text{SH}(^2\Pi)$. Neglecting spin flipping, there are three states that correlate to $\text{S}(^3P)$, two of them connect to the $\text{SH}(^2\Pi)$. These two electronic states are of $^3A'$ and $^3A''$ symmetry, and have been studied in detail by Maiti et al. (2004). Here we use the adiabatic PES calculated by Maiti et al. (2004). Reaction $\text{S} + \text{H}_2 \rightarrow \text{SH} + \text{H}$ is endothermic by ≈ 1.02 eV (without zero-point energy corrections), very similar to the endothermicity of reaction $\text{S}^+ + \text{H}_2 \rightarrow \text{SH}^+ + \text{H}$ (Zanchet et al. 2013a, 2019). The main difference is the presence of a barrier, of ≈ 78 meV (≈ 905 K) with respect to the $\text{SH} + \text{H}$ asymptote.

We performed quantum wave packet calculations for the reactions $\text{S} + \text{H}_2(v=2, 3, j=0)$ and $\text{SH}(v=0, j=0) + \text{H}$. We used MADWAVE3 (Gómez-Carrasco & Roncero 2006; Zanchet et al. 2009) to calculate the reaction probabilities for the initial vibrational state of the diatomic reactant (in the ground state rotational state, $j=0$). We employed the usual partial wave expansion to calculate the reaction cross section. We calculated only few total angular momenta of the triatomic system, $J=0, 10$ and 20 . The other J needed in the partial wave expansion were obtained using the J -shifting-interpolation

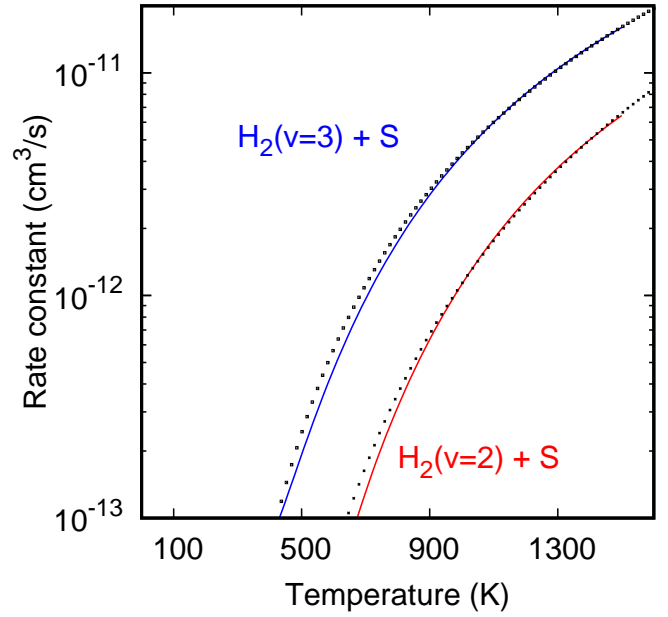


Fig. B.1. Calculated rate constants as a function of temperature for reaction $\text{S}(^3P) + \text{H}_2(v) \rightarrow \text{SH} + \text{H}$. Dotted curves are fits of the form $k(T) = \alpha (T/300)^\beta \exp(-\gamma/T)$. Rate coefficients are listed in Table 1.

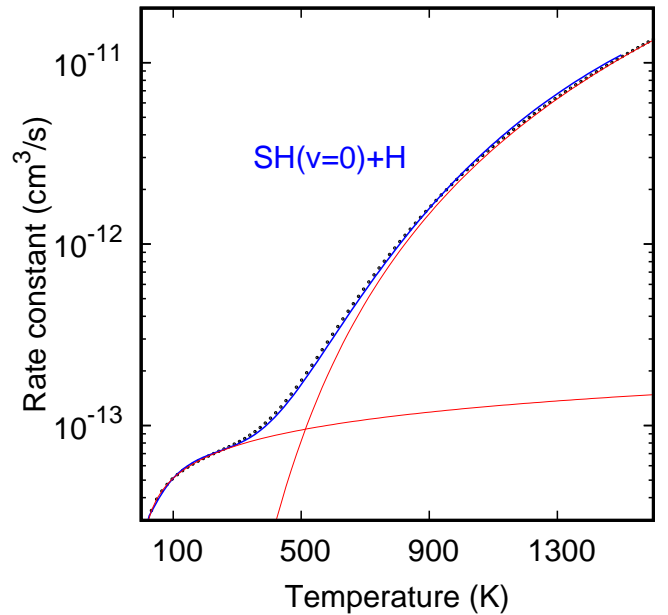


Fig. B.2. Calculated rate constants as a function of temperature for reaction $\text{SH}(v=0) + \text{H} \rightarrow \text{S} + \text{H}_2$. The best fit to the calculated rate requires two Arrhenius-like expressions (one for low temperatures and one for high temperatures). Rate coefficients of these fits are listed in Table 1.

method (see Zanchet et al. 2013a). The initial-state-specific rate constants are obtained by numerical integration of the cross section using a Boltzmann distribution (Zanchet et al. 2013a). The resulting reaction rate constants are shown in Figs. B.1 and B.2. The numerical values of the rate constants are fitted to the usual analytical Arrhenius-like expression (shown as dotted curves). We note that the shoulder in the rate constants of reaction $\text{SH}(v=0) + \text{H}$ requires two functions in the temperature range of 200–800 K. Rate coefficients are tabulated in Table 1.

Appendix C: SH and H₂S photoionization and photodissociation cross sections

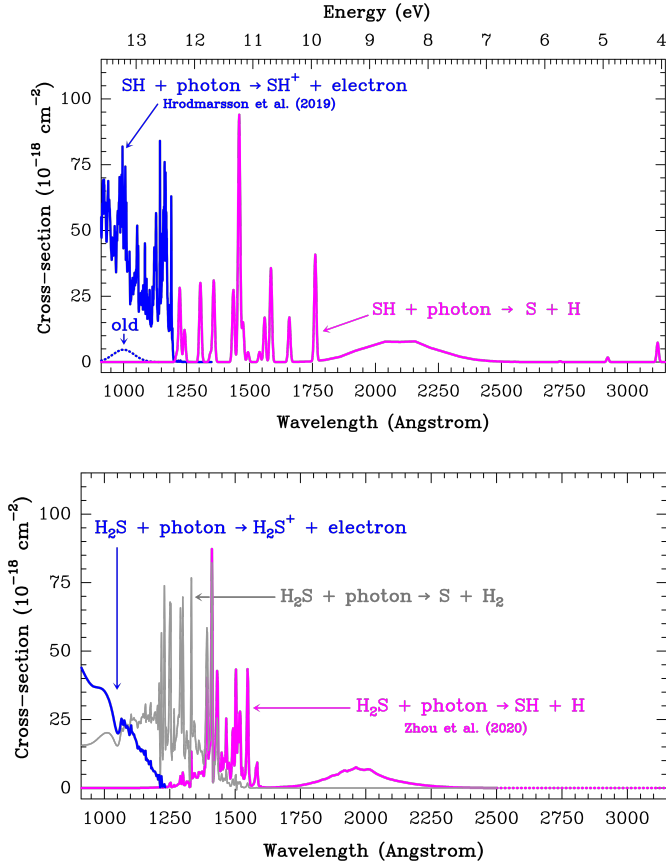


Fig. C.1. Photoionization and photodissociation cross sections. *Top panel:* $\sigma_{\text{ion}}(\text{SH})$ (blue curve from laboratory experiments by Hrodmarsson et al. 2019). The pink curve is $\sigma_{\text{diss}}(\text{SH})$ (Heays et al. 2017, and references therein). *Bottom panel:* $\sigma_{\text{ion}}(\text{H}_2\text{S})$ (blue curve) and $\sigma_{\text{diss}}(\text{H}_2\text{S})$ (gray and pink curves; from Zhou et al. 2020).

Figure C.1 shows the experimental SH and H₂S photoionization and photodissociation cross sections (cm^2) used in our PDR models. We integrate these cross sections over the specific FUV radiation field at each A_V depth of the PDR to obtain the specific photoionization and photodissociation rates (s^{-1}).

Appendix D: H₂S ortho-to-para ratio and T_{spin}

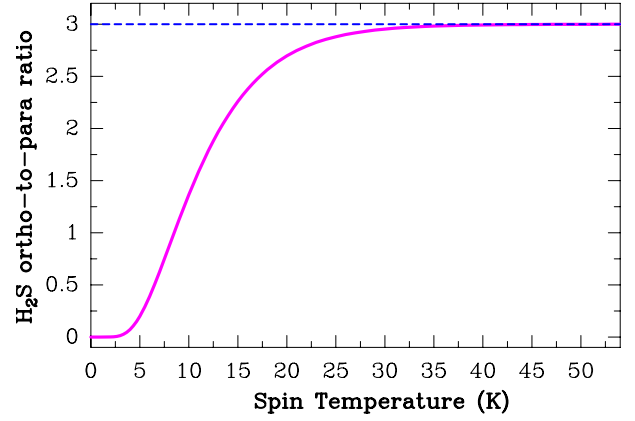


Fig. D.1. OTP ratio of H₂S as a function of spin temperature (Eq. (D.1)).

The OTP ratio is sometimes related to a nuclear-spin-temperature (T_{spin} , e.g., Mumma et al. 1987) defined, for H₂O or H₂S, as:

$$\text{OTP} = \frac{3 \sum (2J+1) \exp(-E_o(J)/T_{\text{spin}})}{\sum (2J+1) \exp(-E_p(J)/T_{\text{spin}})} \quad (\text{D.1})$$

Here, $E_o(J)$ and $E_p(J)$ are the energies (in Kelvin) of *o*-H₂S and *p*-H₂S rotational levels (with the two ground rotational states separated by $\Delta E = 19.8 \text{ K}$). Figure D.1 shows the OTP ratio of the two H₂S nuclear spin isomers as a function of T_{spin} . The OTP ratio we infer toward the DF position of the Bar, 2.9 ± 0.3 , is consistent with the statistical ratio of 3/1, and implies $T_{\text{spin}} \geq 30 \pm 10 \text{ K}$.

Appendix E: Line parameters of IRAM 30 m, ALMA, and SOFIA observations

Table E.1. Parameters of H₂S and H₂³⁴S lines detected with the IRAM 30 m telescope toward three positions of the Orion Bar.

Position	Species	Transition J_{K_a,K_c}	Frequency [GHz]	E_u/k [K]	A_{ul} [s ⁻¹]	S_{ul}	g_u	$\int T_{mb} dv$ [K km s ⁻¹]	v_{LSR} [km s ⁻¹]	Δv [km s ⁻¹]	T_{mb} [K]
(+10, -10)	<i>o</i> -H ₂ S	1 _{1,0} -1 _{0,1}	168.763	8.1	2.68×10^{-5}	1.5	3	18.32 (0.01)	10.5 (0.1)	2.5 (0.1)	7.03
	<i>o</i> -H ₂ ³⁴ S	1 _{1,0} -1 _{0,1}	167.911	8.1	2.62×10^{-5}	1.5	3	1.22 (0.01)	10.5 (0.1)	2.0 (0.1)	0.57
	<i>p</i> -H ₂ S	2 _{2,0} -2 _{1,1}	216.710	84.0	4.87×10^{-5}	2.2	5	0.35 (0.01)	10.4 (0.1)	2.1 (0.1)	0.16
(+30, -30)	<i>o</i> -H ₂ S	1 _{1,0} -1 _{0,1}	168.763	8.1	2.68×10^{-5}	1.5	3	17.16 (0.02)	10.3 (0.1)	2.4 (0.1)	6.85
	<i>o</i> -H ₂ ³⁴ S	1 _{1,0} -1 _{0,1}	167.911	8.1	2.62×10^{-5}	1.5	3	1.28 (0.01)	10.4 (0.1)	1.9 (0.1)	0.63
(+35, -55)	<i>o</i> -H ₂ S	1 _{1,0} -1 _{0,1}	168.763	8.1	2.68×10^{-5}	1.5	3	3.57 (0.02)	9.6 (0.1)	3.1 (0.1)	1.08
	<i>o</i> -H ₂ ³⁴ S	1 _{1,0} -1 _{0,1}	167.911	8.1	2.62×10^{-5}	1.5	3	0.18 (0.02)	9.8 (0.1)	2.7 (0.3)	0.06

Notes. Parentheses indicate the uncertainty obtained by the Gaussian fitting programme.

Table E.2. Parameters of SH⁺ targeted with ALMA toward the DF position.

Position	Species	Transition	Frequency [GHz]	E_u/k [K]	A_{ul} [s ⁻¹]	$\int T_{mb} dv$ [K km s ⁻¹]	v_{LSR} [km s ⁻¹]	Δv [km s ⁻¹]	T_{mb} [K]
(+10, -10)	SH ⁺	$N_J = 1_0-0_1 \ F = 1/2-1/2$	345.858	16.6	1.14×10^{-4}	0.36 ^(a) (0.03)	10.7 (0.2)	2.7 (0.3)	0.12
	SH ⁺	$N_J = 1_0-0_1 \ F = 1/2-3/2$ ^(b)	345.944	16.6	2.28×10^{-4}	0.70 ^(a) (0.03)	10.4 (0.1)	2.5 (0.1)	0.26

Notes. ^(a)Integrated over a 5'' aperture to increase the S/N of the line profiles. ^(b)Line integrated intensity map shown in Fig. 3.

Table E.3. Parameters of SH lines (neglecting HFS) targeted with SOFIA toward the DF position.

Position	Species	Transition	Frequency [GHz]	E_u/k [K]	A_{ul} [s ⁻¹]	$\int T_{mb} dv$ [K km s ⁻¹]	v_{LSR} [km s ⁻¹]	Δv [km s ⁻¹]	T_{mb} [K]
(+10, -10)	SH	$^2\Pi_{3/2} \ J = 5/2^+ - 3/2^-$	1382.911	66.4	4.72×10^{-3}	<1.11 ^(a) (0.20)	12.1 ^(a) (0.8)	7.9 ^(a) (1.3)	0.16
	SH	$^2\Pi_{3/2} \ J = 5/2^- - 3/2^+$	1383.242	66.4	4.72×10^{-3}	<0.34 (0.12)	11.7 (0.5)	2.3 (0.8)	0.14

Notes. ^(a)Uncertain fit.